Passive Post-stall Flow Control on Nonslender Delta Wings Using Flags

Junchen Tan[1], Zhijin Wang[2] and Ismet Gursul[3]

Department of Mechanical Engineering, University of Bath, Bath BA2 7AY, UK

Abstract

The lift force on two nonslender delta wings of sweep angles of $\Lambda = 40°$ and $50°$, with flags attached to the leading-edge, was investigated. Substantial lift enhancement in the post-stall regime of the clean wings and the stall delay were observed. With a flag, the flow field measurements showed the reattachment of the shear layer onto the wing surface and the re-formation of the leading-edge vortex, whereas the clean wing had completely stalled flow at the same angle of attack. Over a wide range of angle of attack, mass ratio, and flag length, the maximum lift enhancement was attained when the dimensionless frequency of flag oscillations was in an optimal range and the flag-tip velocity had sufficient amplitude. The optimal dimensionless frequency range corresponded to the natural shear layer instabilities of the clean wing. The excitation in this range substantially increased the coherency of the separated flow due to the flag oscillations. The main mechanism of the lift increase is the excitation of the shear layer, which exhibits a convective instability. This is very different from the lift enhancement on airfoils for which the flags locks-in to the wake instability, which is known to have an absolute instability at the post-stall angles of attack of the clean airfoil.

1 Ph.D. Student, Department of Mechanical Engineering.
2 Associate Professor, Department of Mechanical Engineering, Senior Member AIAA.
3 Professor, Department of Mechanical Engineering, Fellow AIAA, corresponding author, i.a.gursul@bath.ac.uk

Nomenclature

A	=	peak-to-peak amplitude of flag oscillations, m
C	=	two-point cross-correlation coefficient of flag displacement
C_L	=	time-averaged lift coefficient
$C_{L,max}$	=	maximum lift coefficient
c	=	root chord length, m
E	=	Young's modulus of membrane, Pa
EI	=	bending stiffness of flag, Pa/m^4
f	=	frequency, Hz
h	=	thickness of flag structure, m
h_m	=	thickness of latex membrane sheet, m
h_p	=	thickness of plastic shim, m
K_B	=	dimensionless bending stiffness
L	=	flag length, m
Re	=	Reynolds number based on the chord length
Re_L	=	Reynolds number based on the flag length
St^*	=	Strouhal number based on the projection of the wing chord length, $fc\sin(\alpha)/U_\infty$
s	=	local semi-span of the wing, m
t	=	time, s
t/c	=	thickness-to-chord ratio
U	=	time-averaged streamwise velocity, m/s
U_∞	=	freestream velocity, m/s
V	=	time-averaged cross-stream velocity, m/s
x	=	chordwise coordinate, m
x'	=	coordinate normal to flag and along the wing surface, m
y	=	cross-stream distance from wing surface, m

y'	=	flag cross-stream distance from the wing surface, m
z	=	spanwise coordinate, m
z'	=	flag spanwise coordinate, m
α	=	angle of attack, °
α_s	=	stall angle, °
Λ	=	sweep angle, °
λ	=	wavelength of vortical structure, m
μ	=	structure-to-fluid mass ratio
v	=	kinematic viscosity of fluid, m^2/s
ρ_f	=	density of fluid, kg/m^3
ρ_m	=	density of membrane, kg/m^3
ρ_p	=	density of plastic shim, kg/m^3
ρ_s	=	density of flag structure, kg/m^3
ω	=	vorticity, s^{-1}

I. Introduction

It is well known that increased lift force at high angles of attack can be achieved with active flow control methods applied to nonslender delta wings (typically with sweep angles between $\Lambda = 35°$ and $55°$) [1]. Control of flow separation is easier on nonslender delta wings compared to slender delta wings because of the differences in the leading-edge vortex topology. Unlike for the slender delta wings, reattachment of the separated shear layer onto the wing surface becomes possible. The separation control of three-dimensional shear layers originating from the leading-edge of wings has strong similarities to those of unswept wings. For example, synthetic-jet actuation [2] and pulsed blowing [3] were shown to result in significant lift enhancement in the post-stall regime, whereas for the pre-stall angles of attack there was negligible effect. For both unswept wings and nonslender delta wings, the main mechanism of active flow control relies on the excitation of flow instabilities. Unsteady periodic forcing was found to be generally more efficient in separation control of three-dimensional shear layers than steady (continuous) blowing or suction.

The above studies also identified an optimal range of dimensionless excitation frequencies, fc/U_∞, in the range of 0.5 to 2.0 in the post-stall regime (where f is the frequency, c is the root chord length, and U_∞ is the freestream velocity). Gad-el-Hak and Blackwelder [4] reported that the periodic blowing at the leading-edge at a frequency of approximately half the natural shedding frequency made the leading-edge vortex more coherent. Taylor *et al.* [5] revealed dominant peaks in the spectra of velocity fluctuations due to the shear layer instabilities in the range of $fc/U_\infty = 1$ to 5 at post-stall angles of attack over a 50-deg sweep delta wing. As the three-dimensional vortical structures shed from the leading-edge and evolved (possibly undergoing vortex-merging as well), the dominant peaks varied depending on the chordwise and spanwise location of the probe. It was suggested that the shear-layer structures shed in a conical way, resulting in the dominant frequencies varying with the chordwise and spanwise location of the probe. In a region downstream of the mid-chord and closer

to the mid-span, the dominant frequencies were in the range of $fc/U_\infty = 1$ to 2, which agree with the optimal frequencies found in the active flow control experiments cited above.

Similar observations of enhanced post-stall flow conditions to those of the active flow control experiments were reported for nonslender delta wings subjected to small-amplitude wing motion. These studies also reported similar range of optimal frequencies for both symmetric oscillations (pitching) [6-8] and anti-symmetric oscillations (roll) of wings [8]. The periodic motion of the leading-edge promotes reattachment of the flow on the wing surface. For sweep angles between 30-deg and 50-deg, the reattachment process exhibited generic features and lift enhancement, when the wing was subjected to small-amplitude oscillations.

Flexible nonslender delta wings may exhibit significant lift enhancement in the post-stall region compared to rigid delta wings if the wing flexibility is appropriately selected [5]. The lift enhancement was observed to occur when the wing exhibited vibrations in the torsional structural modes and the structural frequency was close to that of the shear-layer instabilities. The self-excited anti-symmetric vibrations produce similar excitation of the separated shear layer due to the active flow control methods or the motion of the leading-edge of the rigid wings in unsteady forced motion. Using the wing flexibility and the fluid-structure interactions in this case mimic the effects of periodic actuation, while requiring no external power input, hence providing a passive flow control.

Recently it was shown that self-excited oscillations of a small flag attached at the leading-edge of a two-dimensional airfoil at post-stall angles of attack could excite the separated shear layer, induce periodic shedding of leading-edge vortices and lead to increased time-averaged lift force [9]. The frequency of the flag oscillations could be tuned to the frequency of the flow instabilities by properly choosing the properties of the flag [10, 11]. For the case of nominally two-dimensional post-stall flows over airfoils and high-aspect-ratio unswept wings, the main flow instability that flags lock-in

is the wake instability. This article presents experimental results for small flags attached to the leading-edge of nonslender delta wings. The lift enhancement mechanism for nonslender delta wings at post-stall angles of attack exhibits some similarities to those of unswept wings, but also some important differences. The main similarity is that both mechanisms rely on the excitation of flow instabilities as discussed above. The main difference is that, whereas nominally two-dimensional wake instability (known to be an absolute instability [12] for bluff-body wakes) is the key instability for flags on unswept wings to lock-in, there is no evidence that wake instability plays any role for non-sender delta wings. Instead, the experiments with active flow control methods as well as with unsteady wing motion suggest that excitation at the Kelvin-Helmholtz instability (known to be a convective instability [12] for mixing-layers) of the three-dimensional shear layers is the key mechanism.

In this article, we investigate post-stall flow control by using short flags attached to the leading-edge of nonslender delta wings. By using measurements of lift force, flow, and flag deformation, we clarify the mechanism of lift enhancement and which flow instabilities are involved in the fluid-structure interactions. The experiments were focused on two nonslender delta wings with sweep angles of Λ = 40 deg and 50 deg.

II. Methodology

A. Experimental setup

The experiments were conducted in a low-speed, closed-circuit, open-jet wind tunnel located at the University of Bath. A schematic diagram of the half-wing models with leading-edge flags is shown in Figure 1(a). The red dashed lines in Figure 1(a) show the locations of the laser sheets for the flow measurements. The coordinate system x-y-z shows the chordwise, cross-stream, and spanwise coordinate. The origin of the coordinate system is located at the wing apex. The coordinate system x'-y'-z' shows the coordinate normal to flag, normal to the wing surface, and flag spanwise coordinate.

The origin is located at the mid-span of the flag. The wind tunnel has a circular nozzle of 0.76 m in diameter, with a maximum freestream velocity of 30 ms^{-1} and the freestream turbulence intensity of 0.1%. The experimental setup for the particle image velocimetry (PIV) measurements for flow fields and the digital image correlation (DIC) measurements for flag deformation fields are shown schematically in Figure 2. The inset shows the half-wing model with the flag. Two nonslender delta wings (sweep angles $\Lambda = 40°$ and $50°$) were used in the experiments; each wing had a root chord of $c = 200$ mm and a thickness-to-chord ratio $t/c = 0.06$ with a 45° windward bevel angle. The wings were mounted vertically to an aluminum binocular strain-gauge force balance placed beneath the endplate with a small gap of approximately 2 mm between the wing root and the endplate. The freestream velocity was maintained at $U_\infty = 15$ ms^{-1} for all tests, corresponding to a Reynolds number based on the root chord length of $Re = 200,000$.
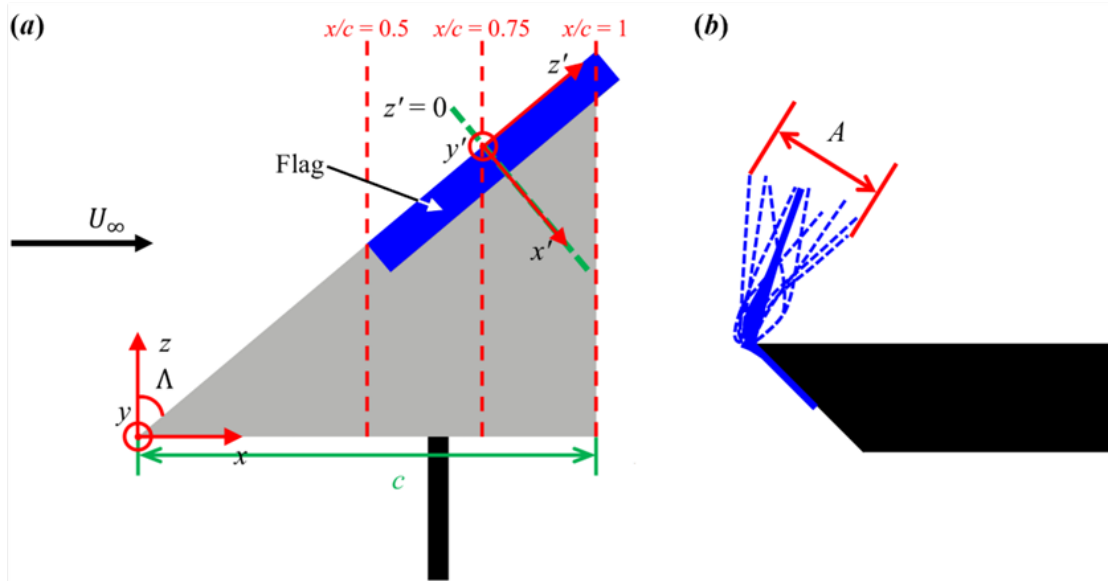

Figure 1: (a) Schematic of the wing-flag assembly; (b) definition of peak-to-peak amplitude A of flag oscillations.

Preliminary experiments suggested that full-span flags attached along the entire leading-edge of the wings are not as effective. This is expected because the flags interact with the three-dimensional vortical structures shed from the leading-edge, which implies varying dominant frequency in the

chordwise and spanwise directions. It is noted that, for a tapered wing with unswept leading-edge and swept trailing-edge [11], both full-span and part-span flags attached to the leading-edge of the wing exhibited significant three-dimensionality and phase-lags. The effect of the three-dimensional flow is expected to be more significant for delta wings. For the delta wing with the sweep angle of 50° in this paper, the initial experiments by varying the span and the chordwise location of the flags revealed that optimal flags covered the 50% of the length of the entire leading-edge of the wing and had the optimal location when placed between the mid-chord and the trailing-edge (aft of the mid-chord, see Figure 1(a)). In Figure 1(b), the blue-dashed lines schematically show the instantaneous flag shapes, whereas the solid blue line indicates the time-averaged flag shape. Both compliant flags and nearly-rigid flags were tested, though our present investigations mainly focus on the nearly-rigid flags as our previous study [10] suggest that nearly-rigid flags are more effective in producing high lift due to better spanwise coherence of the flag oscillations.
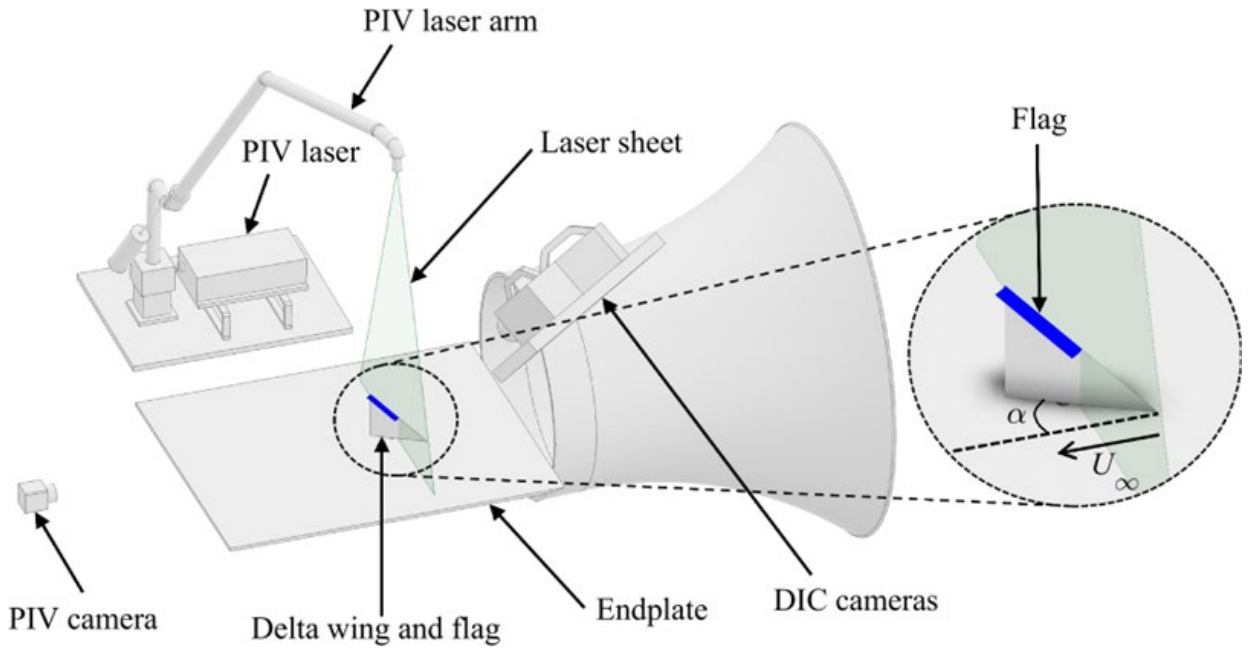

Figure 2: Schematic of experimental setup for particle image velocimetry and digital image correlation measurements.

Compliant flags were made of black latex sheet with thickness of $h_m = 0.2$ mm, Young's modulus of $E = 1.78$ MPa, and density of $\rho_m = 940$ kgm^{-3}; nearly-rigid flags were fabricated based on the latex

membrane done by gluing plastic shims at the trailing portion of the flag, leaving a 5 mm gap between the plastic shims and the leading-edge to form an effective flexible hinge. The plastic shims used had various thicknesses (h_p ranges from 0.05 to 0.25 mm) and densities (ρ_p ranges from 1,433 to 1,470 kgm^{-3}). The structure-to-fluid mass ratio μ, dimensionless bending stiffness K_B, as well as the Reynolds number based on the flag length Re_L are the three key parameters that govern the fluid-flag interactions, which are defined as:

$$\mu = \frac{\rho_s h}{\rho_f L}, \qquad K_B = \frac{EI}{\rho_f U_\infty^2 L^3}, \qquad Re_L = \frac{U_\infty L}{\nu} \tag{1}$$

Here, ρ_s is the density of the flag structure, h is the thickness, L is the length, and EI is the bending stiffness of the flag; ρ_f is the density, and ν is the kinematic viscosity of the fluid.

B. Lift force

The lift force was recorded over a range of angles of attack α from 0° to 40° at 2° increments. The voltage output from the single-axis strain-gauge force balance was amplified through an *Analog Devices* AD624 amplifier and logged to a computer running a custom-developed *LabView* program using a NI6009 data acquisition system (DAQ). The force was measured at a sampling frequency of 1 kHz for 20 s, which was sufficiently long for the mean and the root-mean-square (RMS) of the signal to reach a steady state. The uncertainty in the force measurement was calculated to be $\delta C_L = \pm$ 0.03 based on the methods of Moffat [13]. The drag force was not measured since the primary aim of the present investigation was to study the increase of the lift force and the delay of stall in the post-stall regime.

C. Flag deformation

In order to study the flag deformation, the DIC method was employed. This is a non-intrusive full-field measurement technique by tracking speckling patterns on the surface of an object in time-accurate consecutive image pairs through a correlation method [14,15]. It has been previously used in our laboratory for membrane wings [16], flags on airfoils [9,10], on finite wings [11], and in

freestream [17]. A highspeed DIC system was used to provide time-accurate three-dimensional flag deformation. Two *Photron* FASTCAM SA3 cameras with *Tokina* AT-X Pro D 100 mm F2.8 Macro lenses were mounted normal to the flag capturing images from different viewing angles simultaneously (see Figure 2 for positioning). The LED floodlights were used to illuminate the speckling patterns on the flag. The frame rate of the cameras was set to 1,000 frames per second while the exposure time was set to 1/2000 s to avoid blurred images. For each run, sequences of more than 2,700 consecutive image pairs were captured. The images were processed by the commercial software package VIC3D8. A correlation window of 17 pixels with a grid step size of 4 pixels was used, resulting in an effective grid size around 0.3% of the chord length. The mean and the root-mean-square (RMS) of the fluctuations as well as the proper orthogonal decomposition (POD) modes of the flag displacement were calculated by a custom-developed *MATLAB* code.

D. Flow field

Quantitative flow field analysis was performed using a *TSI* 2D-PIV system. A schematic diagram of the experimental setup of the crossflow (normal-to-freestream) PIV measurements is shown in Figure 2. A double pulse Nd:YAG laser (*Evergreen* EVG00200) with a maximum energy of 200 mJ/pulse was used to illuminate the desired planes. A *TSI* 9307-6 oil droplet generator was used to seed the air with olive oil droplets which have a mean size of 1 μm. The PIV images were captured by a *TSI* PowerView 8MP CCD camera with a *Tokina* AT-X Pro D 100 mm F2.8 Macro lens placed normal to the laser sheet. A *TSI* LaserPulse 610063 synchronizer was used to send signals to the laser and the camera simultaneously. For each measurement 2,000 instantaneous flow fields were captured at a rate of 1 Hz. The commercial software package *TSI* Insight4G and a Hart cross-correlation algorithm were used to calculate the velocity vectors. The interrogation window size was 64×64 pixels, then reduced to 32×32 pixels. The effective grid size was around 0.6% of the chord length. The uncertainty of the velocity measurements was estimated to be within 2% of the freestream velocity. The time-averaged

flow fields as well as the POD modes were obtained from the instantaneous images. The POD analysis was performed using the *OPENPIV POD TOOLBOX* [18].

In the present investigation, we measured the flow at three different types of planes. These include planes that are normal to the freestream, normal to the wing surface, and parallel to the wing surface to capture the near-surface flow at a distance of 1.5% of the chord length from the wing surface. For the normal-to-freestream crossflow measurements, the laser sheets were illuminated from above the wing with the use of a *TSI* LaserPulse Light Arm 610015 to minimize reflection noise on the wing surface at x/c = 0.5, 0.75 and 1.0 (see Figure 1) and the camera was placed downstream of the wing (as sketched in Figure 2). For the planes normal-to-wing surface, the laser sheet was at the mid-span of the flag (intersecting the leading-edge at x/c = 0.75) and was normal to the wing surface, while the PIV camera was oriented as normal to the laser illumination plane.

Hot-wire measurements were conducted for the spectral analysis of the velocity fluctuations over the 50° sweep wing. The *TSI* hot-wire system consisted of a 1750 constant temperature anemometer, a 1150 standard probe support and a 1210-T1.5 hot-wire probe. The fluctuations of the flow velocity were recorded at a sampling frequency of 6 kHz for 60 s at each location. The same signal amplifying and data logging system as for lift force measurements was used. A fast Fourier transform (FFT) algorithm implemented in *MATLAB* was used to calculate the spectra of the velocity fluctuations.

III. Results and discussion

A. Clean wings

Figure 3 presents the time-averaged lift coefficient C_L as a function of angle of attack α for the baseline clean wings. The 50° sweep wing stalls at α_s = 24° with a maximum lift coefficient $C_{L,\max}$ = 0.85. The results show close agreement with literature [19], tested at a similar Reynolds number of Re = 210,000, for a sharp leading-edge and the same bevel angle of the leading-edge. There are slight

differences in the stall angle and the post-stall lift coefficients. For the 40° sweep wing, the stall angle is $\alpha_s = 20°$, with the corresponding maximum lift coefficient of $C_{L,max} = 0.79$. The present study is compared with data in Taylor *et al.* [5] which was tested at $Re = 440,000$, and similar lift gradient can be seen for the pre-stall angles of attack. Although the Reynolds number is more than twice, the effect of Reynolds number is not significant in this range. We note that the $\Lambda = 40°$ wing produces non-zero lift at zero angle of attack for both Reynolds numbers, which is believed to be the camber effect of the beveled leading-edge for this lower sweep angle.
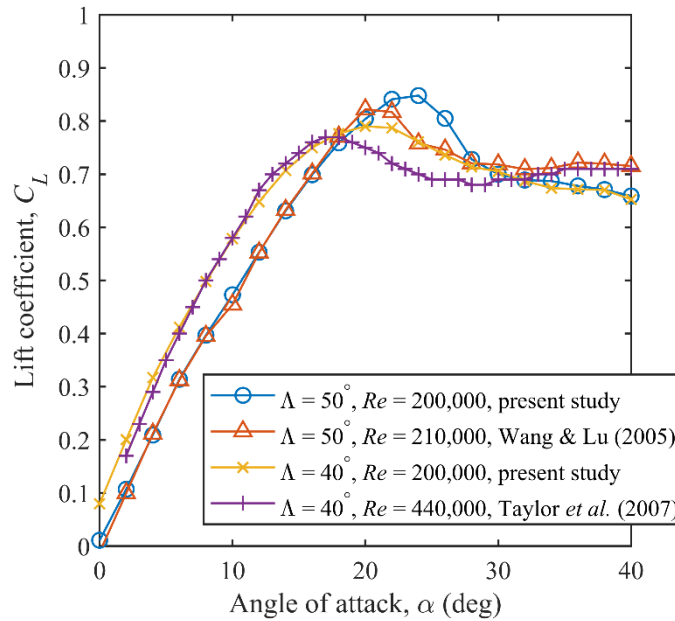

Figure 3: Time-averaged lift coefficient C_L as a function of angle of attack α for clean wings and comparison with the literature.

B. Lift enhancement with flags

The variation of the time-averaged lift coefficient C_L as a function of angle of attack is shown in Figure 4 for the $\Lambda = 50°$ wing with different nearly-rigid flags of varying mass ratio at a fixed flag length of $L/c = 0.1$. The lift curve gradients at small angles of attack are similar to the baseline case. In the post-stall regime, most of the $L/c = 0.1$ nearly-rigid flags provide a benefit of increased lift and delayed stall, except for the heaviest flag of $\mu = 34.0$. The lift enhancement diminishes with increasing mass ratio for the flags. Figure 4 reveals that the $\mu = 10.0$ flag has a maximum lift coefficient of $C_{L,max}$

= 1.07 and a stall angle of $\alpha_s = 30°$. The improvements are significant as they represent a 26% increase in the maximum lift coefficient compared to the baseline (and 53% at the same angle of attack of $\alpha = 30°$) and a delay of the stall angle by 6°. We measured the flow fields with this flag ($\mu = 10.0$, $L/c = 0.1$ flag) at $\alpha = 30°$, which is the stall angle of the wing with this flag.
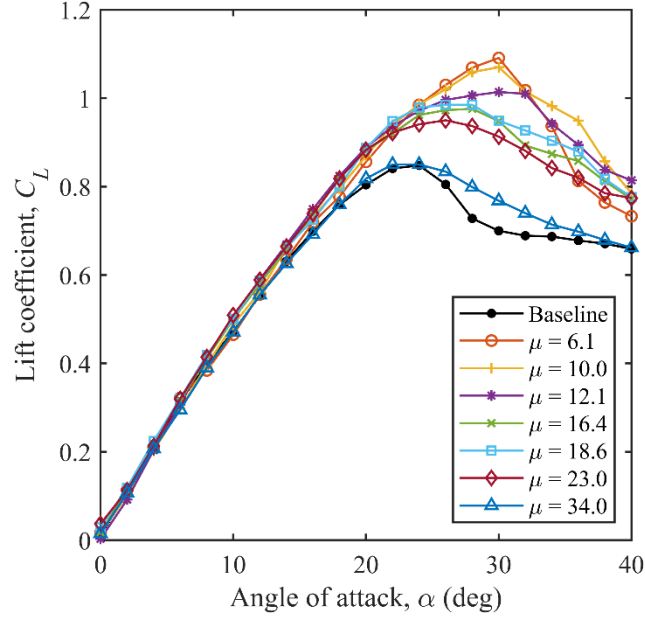

Figure 4: Time-averaged lift coefficient C_L as a function of angle of attack α for different flags of varying mass ratio for fixed flag length $L/c = 0.1$; $\Lambda = 50°$.

In Figure 5, for the clean wing at $\alpha = 30°$ (shown at the top), a representative instantaneous vorticity field in the x'-y' plane normal-to-wing surface and intersecting the leading-edge at $x/c = 0.75$ (see Figure 1) is shown. The corresponding representative vorticity fields with those for the nearly-rigid flag $\mu = 10.0$, $L/c = 0.1$ at $\alpha = 30°$ are shown at the bottom row when the flag tip is closest to the wing surface (left) and furthest from the wing surface (right). For the clean wing in this plane close to the wing-tip (top image), the shear layer separated from the leading-edge indicates a massively stalled flow over the wing. With the flag, the shear layer rolls-up closer to the surface and the separated region looks smaller. When the flag is closest to the wing surface (left image), the flow does not appear to be attached to the flag upper surface and a small vortex rolls-up near the flag tip. There is no indication that the small vortex rolls-up into a larger coherent vortex when the flag-tip is furthest

away from the wing surface (right image). Nevertheless, the indication of the smaller separated region is clear. The crossflow measurements at the planes normal to the freestream are presented next.
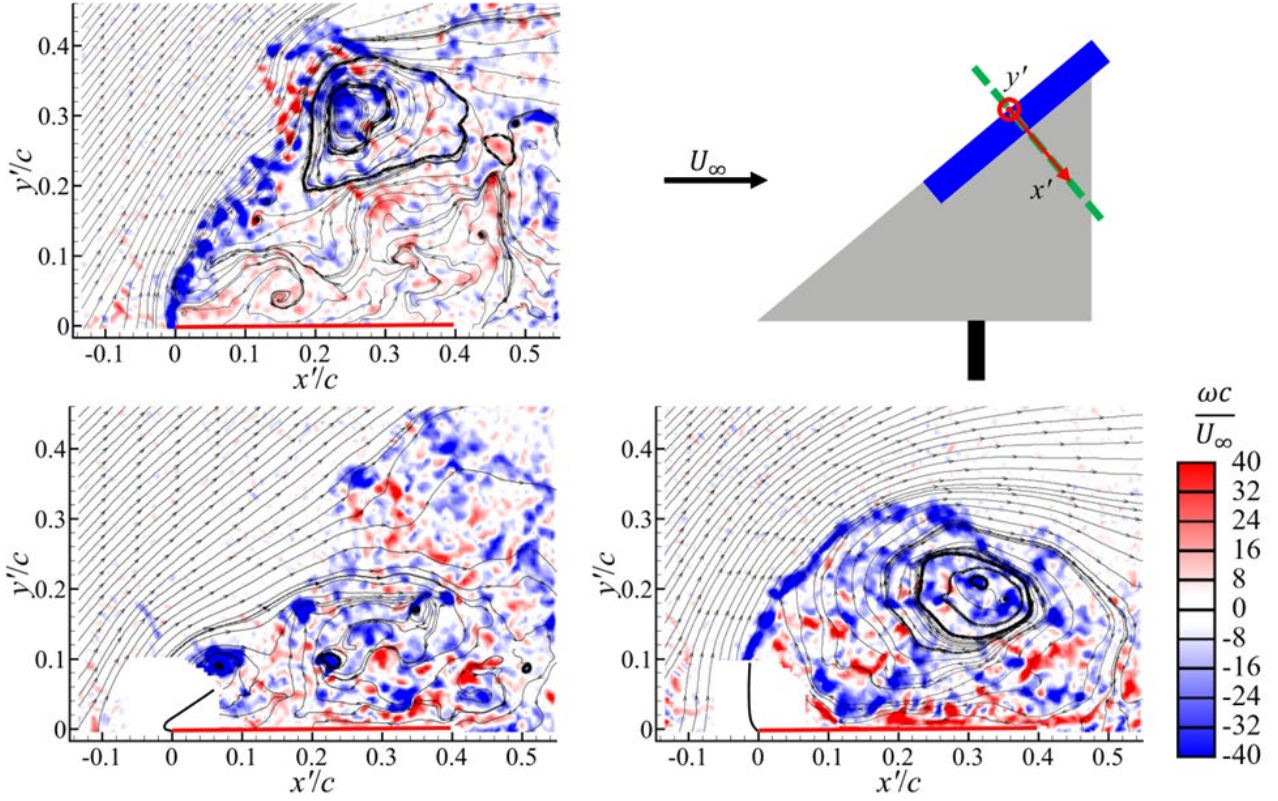

Figure 5: Instantaneous vorticity contours for baseline wing (top) and with flags together with instantaneous flag shapes when the flag-tips are near the extrema (bottom) for $\mu = 10.0$, $L/c = 0.1$ flag, at $\alpha = 30°$, $\Lambda = 50°$.

The time-averaged vorticity contours at the three planes ($x/c = 0.5$, 0.75, and 1.0) normal to the freestream are shown in Figure 6 to demonstrate the effect of flag oscillations on the flow field. The flow field for the clean wing is measured for comparison; the nearly-conical shear layer separates from the leading-edge, reaching the symmetry plane and interacting with the root-plate. Overall, the vorticity magnitude in the shear layer is relatively small, and the flow near the wing surface is weak, consistent with a fully stalled flow at this angle of attack. The streamlines spiral out in the recirculation region for the baseline case, consistent with the complete breakdown of the vortex. When a leading-edge flag is attached (the time-averaged flag shape is also shown), the flow reattaches to the wing surface. A strong streamwise vortex is observed over the upstream stations of the wing,
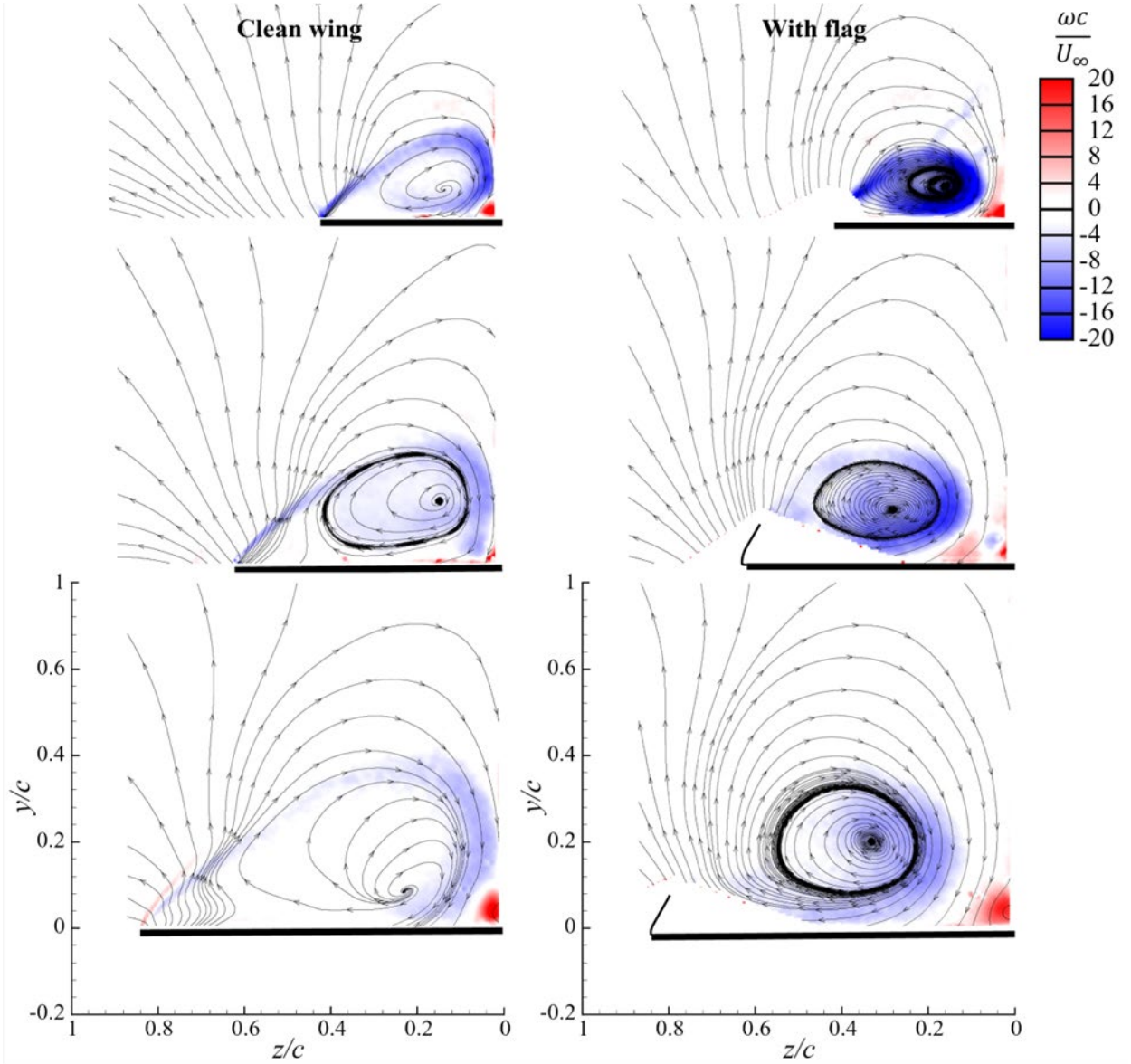
Figure 6: Time-averaged vorticity contours superimposed with time-averaged streamlines for crossflow planes normal to the freestream; top: $x/c = 0.5$, middle: $x/c = 0.75$, and bottom: $x/c = 1$. Left: clean wing, right: $\mu = 10.0$, $L/c = 0.1$ flag; at $\alpha = 30°$, $\Lambda = 50°$.

although it is significantly weakened in the last plane ($x/c = 1.0$), suggesting vortex breakdown in the neighborhood of the trailing-edge. In each plane, the center of the recirculation region moves outboard together with the reattachment line on the wing surface. It is noted that the plane at $x/c = 0.5$ corresponds to the most upstream location of the flag (see Figure 1(a) for a clear illustration), yet the excitation by the oscillating flag downstream has already caused the re-formation of the leading vortex upstream. Similarly, the effectiveness of pulsed-blowing from a finite-span slot located

between $x/c = 0.375$ and 0.625 was reported by Williams *et al.* [3]. We also note that, the present results are qualitatively similar to those reported by Taylor *et al.* [5] where the excitation introduced by the vibrations of the wing leading-edge (the structural modes suggested larger vibration amplitudes aft of the mid-chord).
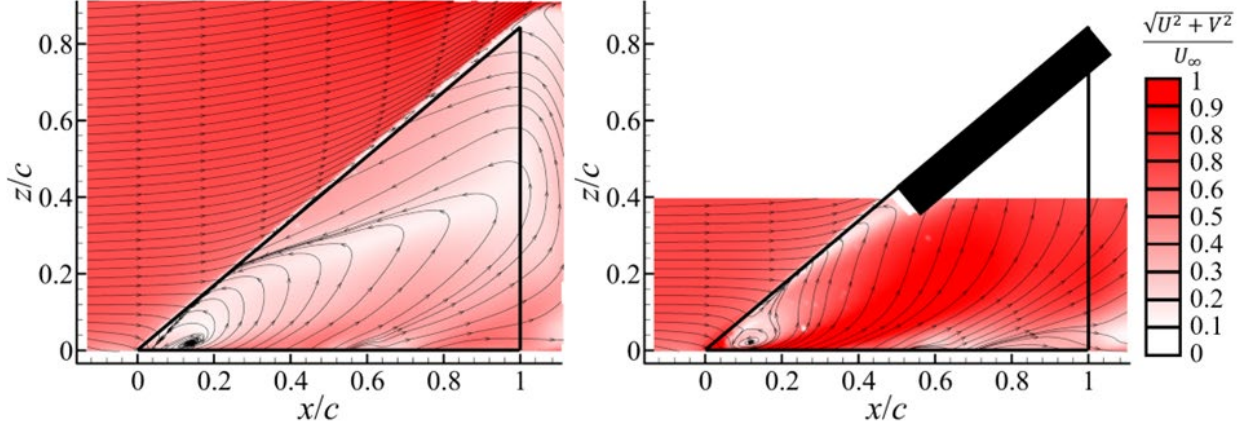

Figure 7: Time-averaged near-surface velocity magnitude contours superimposed with time-averaged streamlines; left: clean wing; right: $\mu = 10.0$, $L/c = 0.1$ flag, $\alpha = 30°$, $\Lambda = 50°$.

The time-averaged near-surface velocity measurements for the baseline wing and with the $\mu = 10.0$, $L/c = 0.1$ nearly-rigid flag for $\alpha = 30°$ are shown in Figure 7. There is a large region of reversed flow on the wing surface for the baseline case (left image); the surface flow pattern is similar to the uncontrolled case in Williams *et al.* [3] at the same angle of attack. The velocity magnitude becomes higher near the surface when the flag is attached (right image). Especially, near the wing centerline the flow is reenergized by the reattachment of the shear layer.

C. Pre-stall versus post-stall angles of attack

The lift enhancement at the post-stall angles of attack in Figure 4 is in contrast with the observations at the pre-stall angles of attack for this flag ($\mu = 10.0$, $L/c = 0.1$) and other flags. Whereas there is qualitative similarity of the lift curves for flags on two-dimensional airfoils, the flow physics are different at pre-stall angles of attack. With the flow separation from the sharp leading-edge for the

nonslender delta wing, there is always separated flow. We observe flag oscillations at the pre-stall angles of attack. Yet, there is virtually no lift increase. Figure 8 compares the power spectral density of the flag-tip displacement fluctuations at a pre-stall angle of attack ($\alpha = 10°$) and at the stall angle ($\alpha = 30°$). For both angles of attack, the flag oscillation frequency is approximately the same, but reveals some change in the dominant frequency near the downstream edge of the flag (near the trailing-edge and the wing-tip). This may be due to the vortex shedding from the trailing-edge.
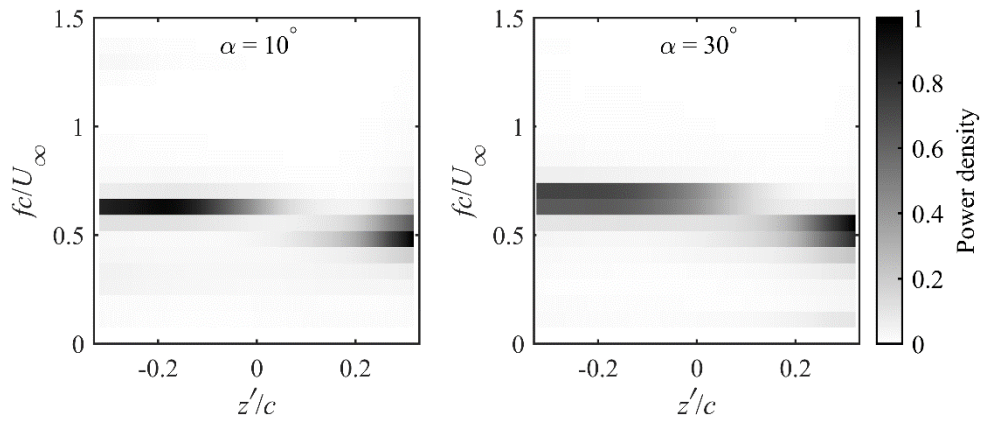

Figure 8: Carpet plot of spectra of flag-tip displacement ($x'/L = 1$) as a function of dimensionless reduced frequency and flag spanwise distance z'/c for $\mu = 10.0$, $L/c = 0.1$ flag; left: $\alpha = 10°$, right: $\alpha = 30°$, $\Lambda = 50°$.

Figure 9 presents the RMS and the first three POD modes of the flag displacement field for the $\mu = 10.0$, $L/c = 0.1$ flag at $\alpha = 10°$ and $30°$. The fraction of energy of the POD modes is plotted in Figure 9(c) as a function of mode number. The first three modes have most of the total energy. At $\alpha = 30°$ the flag has a slightly larger vibration amplitude across the flag span as well as in the region near the wing tip. The first POD modes for the two angles of attack are not notably different as they represent "first-beam-mode" while the second and the third modes indicate spanwise modes. These results suggest that the flag deformations exhibit some three-dimensionality along the span.
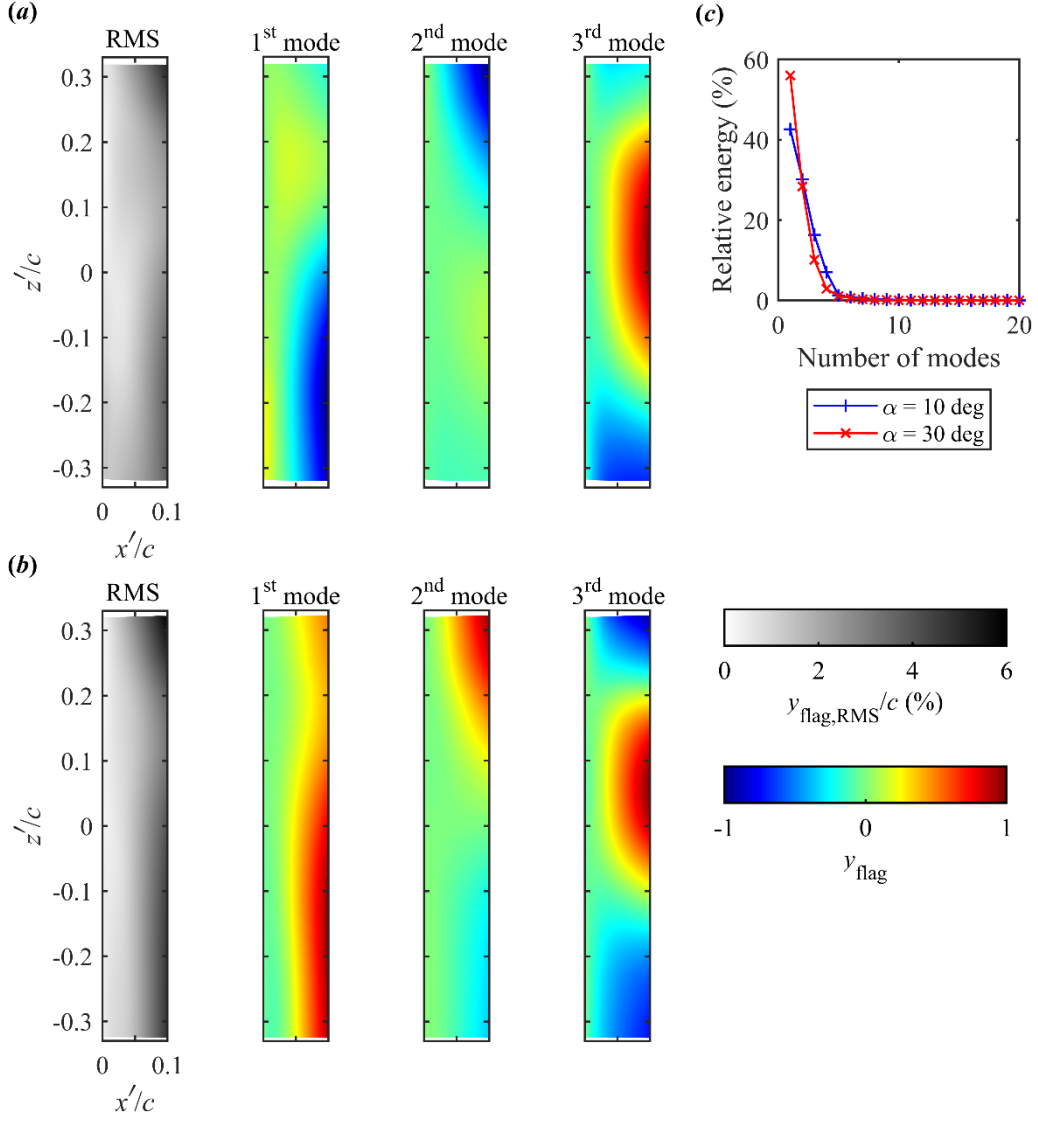
Figure 9: RMS and the first three POD modes of flag displacement for $\mu = 10.0$, $L/c = 0.1$, (a) $\alpha = 10°$, (b) $\alpha = 30°$; and (c) energy fraction as a function of mode number; $\Lambda = 50°$.

The degree of two-dimensionality can be measured by examining the two-point cross-correlation coefficient [20] of the flag-tip displacement as a function of the flag spanwise distance z'/c and is presented in Figure 10. It is defined as

$$C = \frac{\overline{y'_A y'_B}}{\sqrt{\overline{y'^2_A}} \sqrt{\overline{y'^2_B}}} \tag{2}$$

Here, y'_A is the fluctuating flag tip displacement at a reference point, which is selected as the flag-tip at the most upstream location, and y'_B is any arbitrary location along the flag-tip. For both angles of attack, the cross-correlation coefficient decays quickly, indicating three-dimensional flag

displacements. For $\alpha = 10°$ the cross-correlation coefficient decreases to -0.17 at about $0.5c$ from the upstream edge (equivalent to $5L$) and then briefly restores to 0.24 at the downstream edge. The fast decay for the $\alpha = 30°$ starts slightly further from the upstream edge, and the cross-correlation coefficient maintains above 0.9 for $-0.33 \leq z'/c \leq 0.1$ and remains relatively constant around 0.12 between $z'/c = 0.2$ and 0.33.
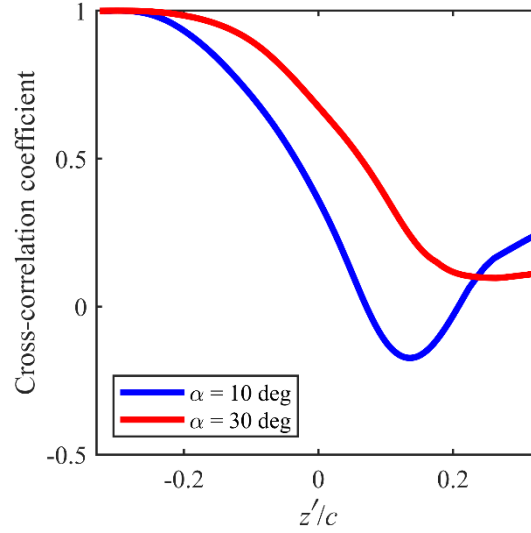

Figure 10: Two-point cross-correlation coefficient of the flag-tip displacement fluctuation as a function of flag spanwise distance z'/c for $\mu = 10.0$, $L/c = 0.1$ flag for $\alpha = 10°$ and $30°$; $\Lambda = 50°$.

For both angles of attack ($\alpha = 10°$ and $30°$), the flag oscillations are qualitatively similar, including approximately the same oscillation frequency. Yet, the time-averaged lift force for the pre-stall angle of attack does not change much since there is already reattached flow on the wing surface. The excitation may modify the reattachment location slightly, but this does not cause any significant changes in the lift force. A similar observation of small change in the reattachment location was reported when a nonslender delta wing was subjected to the small-amplitude roll oscillations at a pre-stall angle of attack [8]. We extended the deformation measurements to a range of angles of attack between 10° and above 30° for the same flag. Figure 11 shows the variation of the change of lift coefficient, dimensionless frequency of the flag-tip oscillations, normalized oscillation amplitude A/c, and the Strouhal number based on the peak-to-peak amplitude at the mid-span of the flag as a function

of angle of attack α for $\mu = 10.0$, $L/c = 0.1$. Here the Strouhal number, fA/U_∞, represents the ratio of the flag-tip velocity to the freestream velocity (see the definition of A in Figure 1(b)), serving as an amplitude parameter. The amplitude parameter, fA/U_∞, and the amplitude A increase slightly with angle of attack across the angle of attack range but cannot increase the lift force at the pre-stall angle of attack because of already reattached flow on the wing surface.
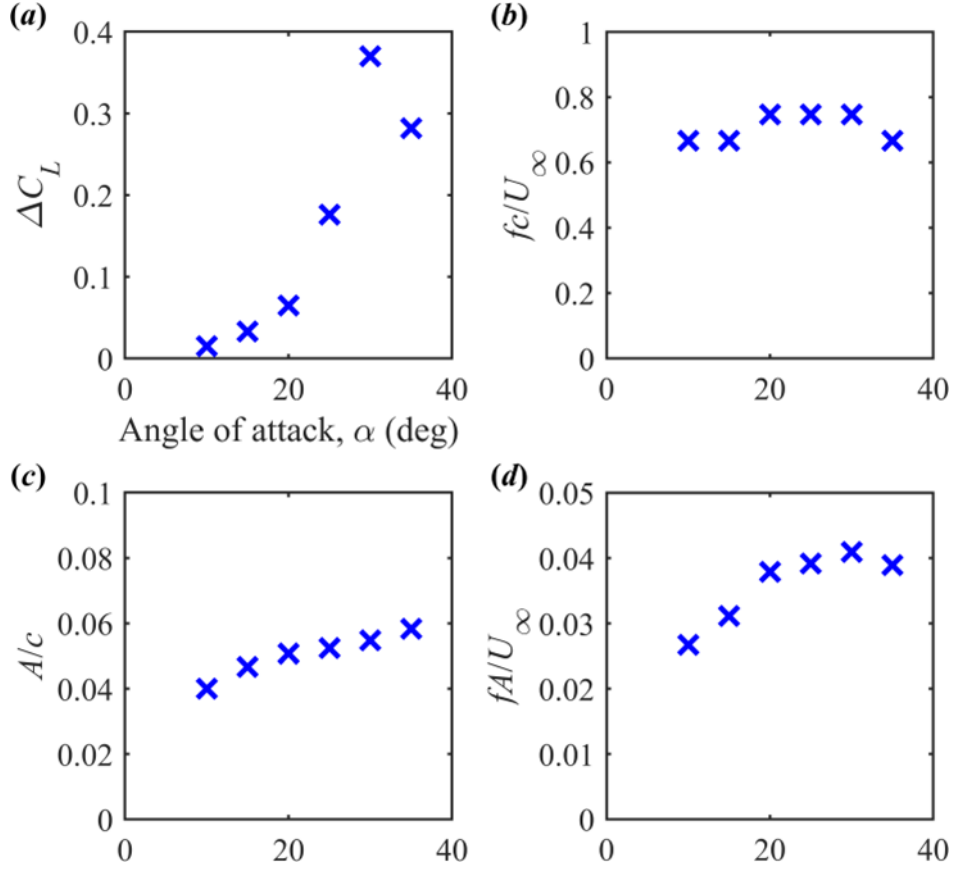

Figure 11: Variation of (a) change of lift coefficient, (b) dimensionless frequency, (c) normalized oscillation amplitude, (d) Strouhal number based on the flag peak-to-peak amplitude as a function of angle of attack α for $\mu = 10.0$, $L/c = 0.1$ flag; $\Lambda = 50°$.

While the lift enhancement increases in the post-stall angle of attack and has a local maximum at $\alpha = 30°$, the dimensionless flag frequency remains roughly constant. This is fundamentally different from the flags on airfoils, for which flag frequency depends on the airfoil angle of attack as the frequency of the wake instability varies (since the effective wake width varies) [10]. For the leading-edge separation on the nonslender delta wing, there is no evidence of locking-in to the wake, which has an absolute instability. The nearly constant frequency for the same flag properties suggests that the

measured frequency corresponds to the natural frequency of the flag. (We note that, for nominally two-dimensional flags in uniform freestream, the flag natural frequency can be predicted by a reduced order model [17] and depends on the mass ratio only if the flag is assumed to be rigid). The hypothesis is that the flag oscillates at the natural structural frequency as it is buffeted by the unsteady separated shear layer and in turn excites the convective instability of the shear layer. We will show that, if the flag properties are selected appropriately and tuned to the natural frequency of the shear layer, aerodynamic performance can be enhanced.

D. Effect of mass ratio

The frequency of the flag oscillations could be tuned to the frequency of the flow instabilities by appropriate selection of the main property of the flags, which is the mass ratio. This is clearly seen in Figure 4, in which the effect of varying the mass ratio is shown on the time-averaged lift coefficient for a fixed flag length of $L/c = 0.1$ for $\Lambda = 50°$. There is a trend of diminishing lift increase with increasing mass ratio for the flags. In the following, we fix the angle of attack at $\alpha = 30°$ and examine the frequency and the amplitude of the flag oscillations with varying mass ratio.
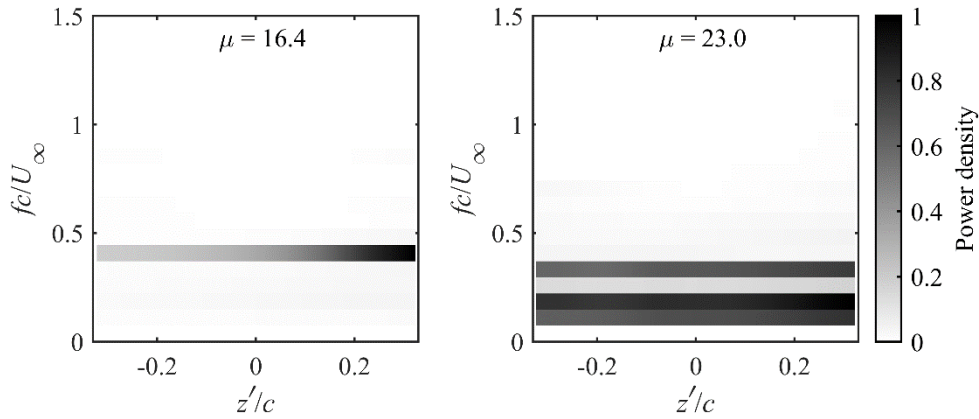

Figure 12: Carpet plot of spectra of flag-tip displacement as a function of Strouhal number and flag spanwise distance z'/c for $L/c = 0.1$ flags for $\alpha = 30°$ and $\Lambda = 50°$; left: $\mu = 16.4$, right: $\mu = 23.0$.

Figure 12 shows the frequency spectra of the flag-tip displacement at the mid-span for the $\mu = 16.4$ and $\mu = 23.0$ flags at $\alpha = 30°$. It is noted that, for the $\mu = 23.0$ flag, there are two dominant frequencies $fc/U_\infty = 0.22$ and 0.37 (likely to be the second harmonic) while the lower frequency has much larger

magnitude. In contrast, the carpet plot for the $\mu = 16.4$ flag contains only one band at $fc/U_\infty = 0.44$. Both the $\mu = 16.4$ and $\mu = 23.0$ flags show improved spanwise uniformity compared to the $\mu = 10.0$ flag in Figure 8.
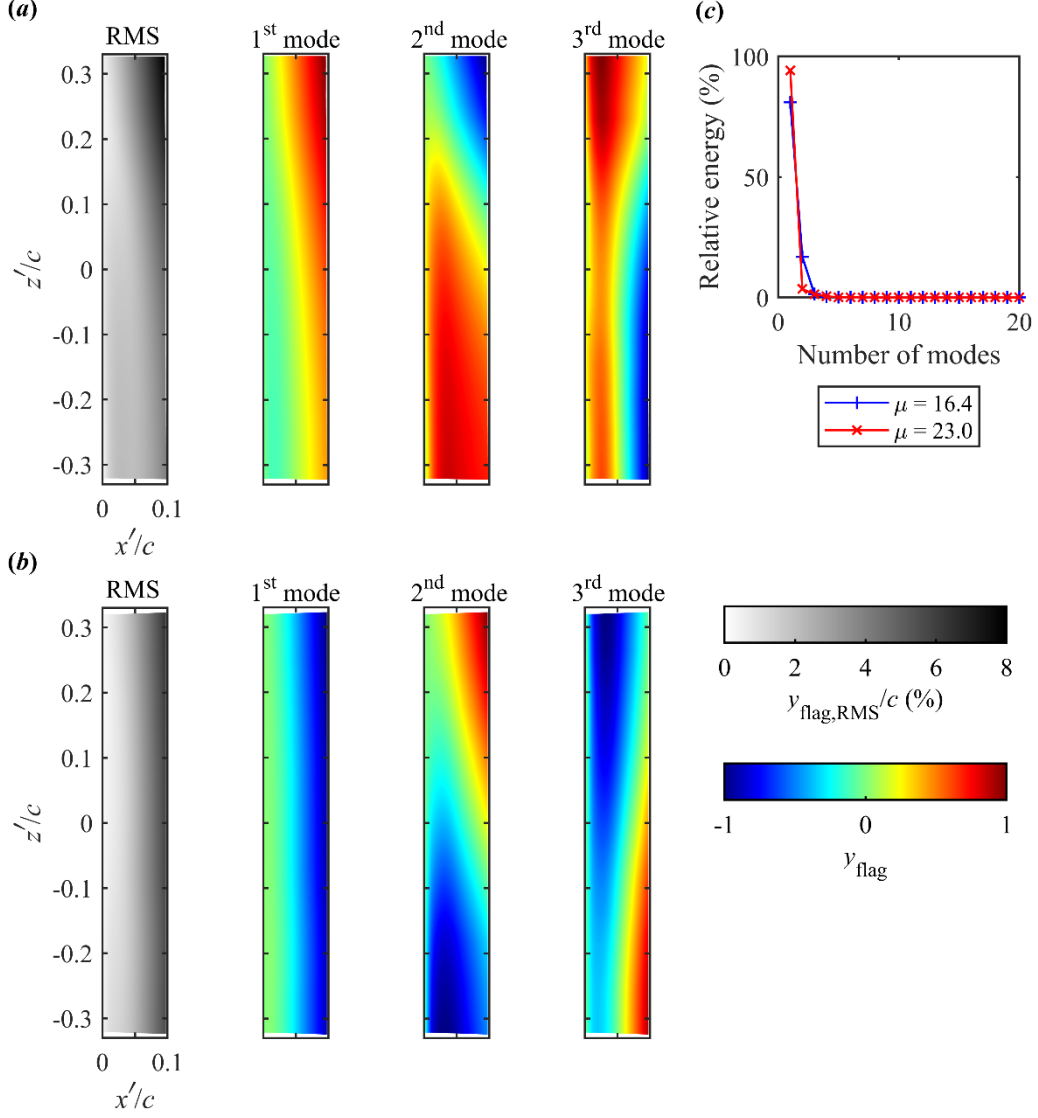

Figure 13: RMS and the first three POD modes of flag-tip displacement for $\alpha = 30°$, (a) $\mu = 16.4$, (b) $\mu = 23.0$; and (c) fraction of energy as a function of mode number; $L/c = 0.1$, $\Lambda = 50°$.

Figure 13 presents the RMS and the first three POD modes of flag-tip displacement for $\mu = 16.4$ and $\mu = 23.0$ at $\alpha = 30°$ and $\Lambda = 50°$. The fraction of energy shown in part (c) as a function of mode indicates that, for both flags, most of the energy is concentrated in the first POD mode. For the $\mu = 23.0$ flag, both the RMS and the first POD mode appear much more two-dimensional. The RMS displacement contours indicate that the flag vibration amplitude near the wing-tip is larger for the μ

= 16.4 flag, although this effect is less significant for the μ = 23.0 flag. Again, we examine the two-point cross-correlation coefficient for the two flags to quantify their spanwise two-dimensionality (see Figure 14). These two flags with higher mass ratios (compared to μ = 10.0 in Figure 10) exhibit significantly better two-dimensionality. Clearly, the spanwise uniformity improves significantly with increasing mass ratio, which is expected to improve the coherence of the excitation. Surprisingly, the lift enhancement decreases with increasing mass ratio (see the lift coefficients in Figure 4).
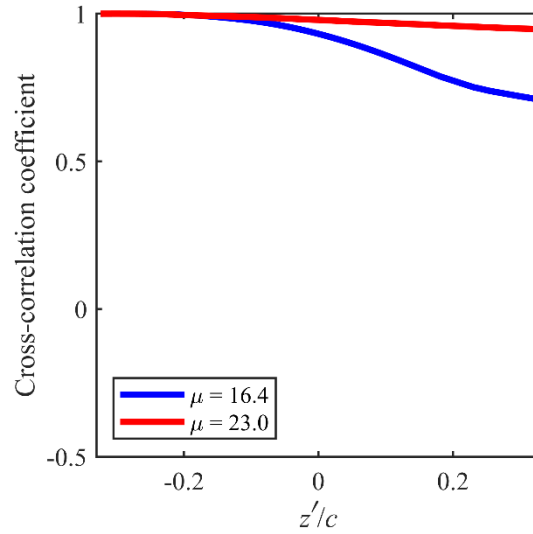

Figure 14: Two-point cross-correlation coefficient of the flag displacement fluctuation at $x'/L = 1$ as a function of flag spanwise distance z'/c for $L/c = 0.1$ flags at $\alpha = 30°$ with $\mu = 16.4$ and $\mu = 23.0$; $\Lambda = 50°$.

Figure 15 shows the variation of the change of lift coefficient, dimensionless frequency, normalized oscillation amplitude, and Strouhal number based on the flag peak-to-peak amplitude as a function of mass ratio for $L/c = 0.1$, $\alpha = 30°$, $\Lambda = 50°$. With increasing mass ratio, both the lift reduction and the dimensionless frequency decrease. It is noted that the decrease in the flag frequency is expected since it scales as

$$\frac{fL}{U_\infty} \propto \mu^{-\frac{1}{2}} = \left(\frac{\rho_s h}{\rho_f L}\right)^{-\frac{1}{2}} \tag{3}$$

for a flag in freestream [17]. For the largest increase in the lift coefficient (for the smallest mass ratio in Figure 15), the dimensionless frequency fc/U_∞ approaches unity, which is consistent with the optimal frequency range reported for various forms of excitation for this sweep angle. The direct

correlation between the lift increase and the flag dimensionless frequency is obvious, although the amplitude parameter of the excitation, fA/U_∞, is also large for the maximum lift enhancement. This suggests that both the dimensionless frequency fc/U_∞ and the amplitude parameter fA/U_∞ are likely to be important. Further evidence to support this conclusion will be presented in the next section.
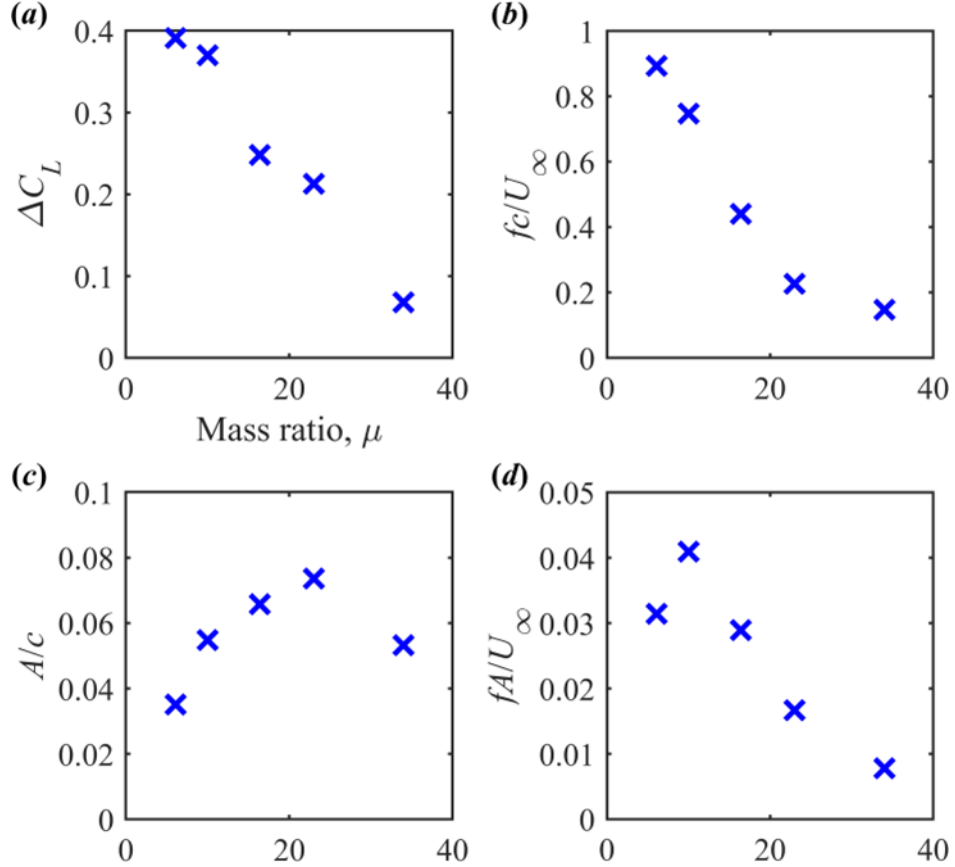

Figure 15: Variation of (a) change of lift coefficient, (b) dimensionless frequency, (c) normalized oscillation amplitude, (d) Strouhal number based on the flag peak-to-peak amplitude as function of mass ratio for $L/c = 0.1$, $\alpha = 30°$, $\Lambda = 50°$.

E. Effect of flag length

As the flag oscillation frequency is expected to depend on the flag length (see the scaling of fL/U_∞ in the above equation), it will have a direct influence on the lift enhancement. In addition, the flag length is likely to affect the formation, shedding, and the release location of the leading-edge vortex. The time-averaged lift coefficient C_L as a function of angle of attack α for nearly-rigid flags with various lengths is presented in Figure 16. The corresponding values of the mass ratio are given in the legend

of the figure. Longer flags or shorter flags are not as effective as $L/c = 0.075$ and 0.1. The longest and shortest flags neither produce a higher maximum lift coefficient than the baseline case nor delay the stall angle.
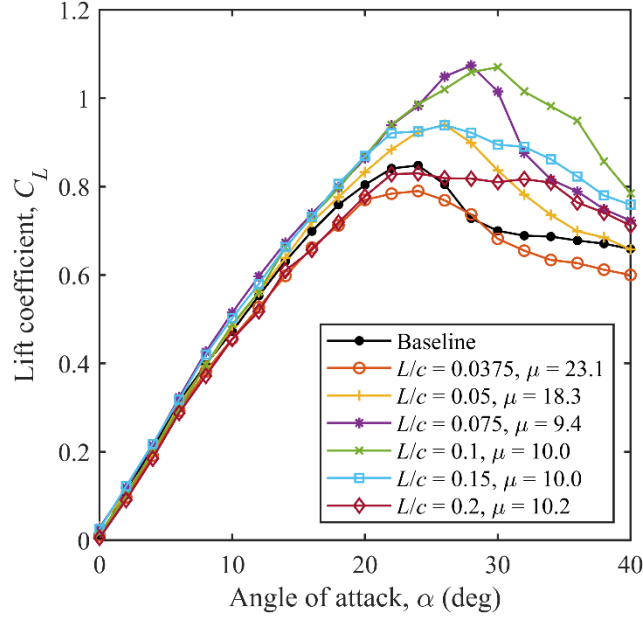

Figure 16: Time-averaged lift coefficient C_L as a function of angle of attack α for flags with different lengths, $\Lambda = 50°$.
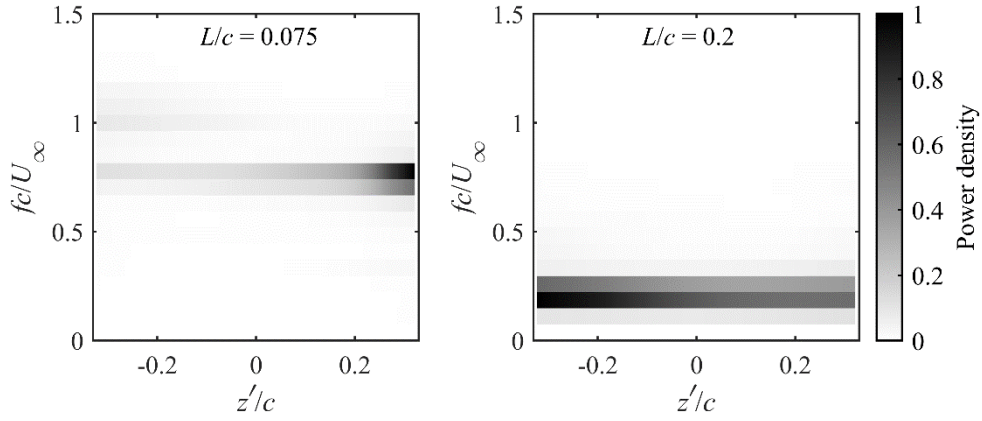

Figure 17: Carpet plot of spectra of flag-tip displacement as a function of flag spanwise distance z'/c, for $L/c = 0.075$ (left) and $L/c = 0.2$ (right); $\alpha = 30°$, $\Lambda = 50°$.

In Figure 17, for $\alpha = 30°$ and $\Lambda = 50°$, we compare the spectra of flag-tip oscillations at the flag-tip as a function of the flag spanwise distance for $L/c = 0.075$ and $L/c = 0.2$. Note that these two flags were designed to have similar mass ratios by adjusting the number and thickness of the plastic shims.

Figure 17 shows that the dimensionless frequencies are $fc/U_\infty = 0.81$ and 0.22, respectively. For the $L/c = 0.075$ flag, there is much larger nonuniformity of the amplitude of the dominant frequency in the spanwise direction (particularly near the upstream edge of the flag) compared to the $L/c = 0.2$ flag. Yet, there is very little lift enhancement for $L/c = 0.2$. This is further evidence that how close the flag oscillation frequency is to the frequency of the natural shear layer instabilities is the most important factor in the lift enhancement.
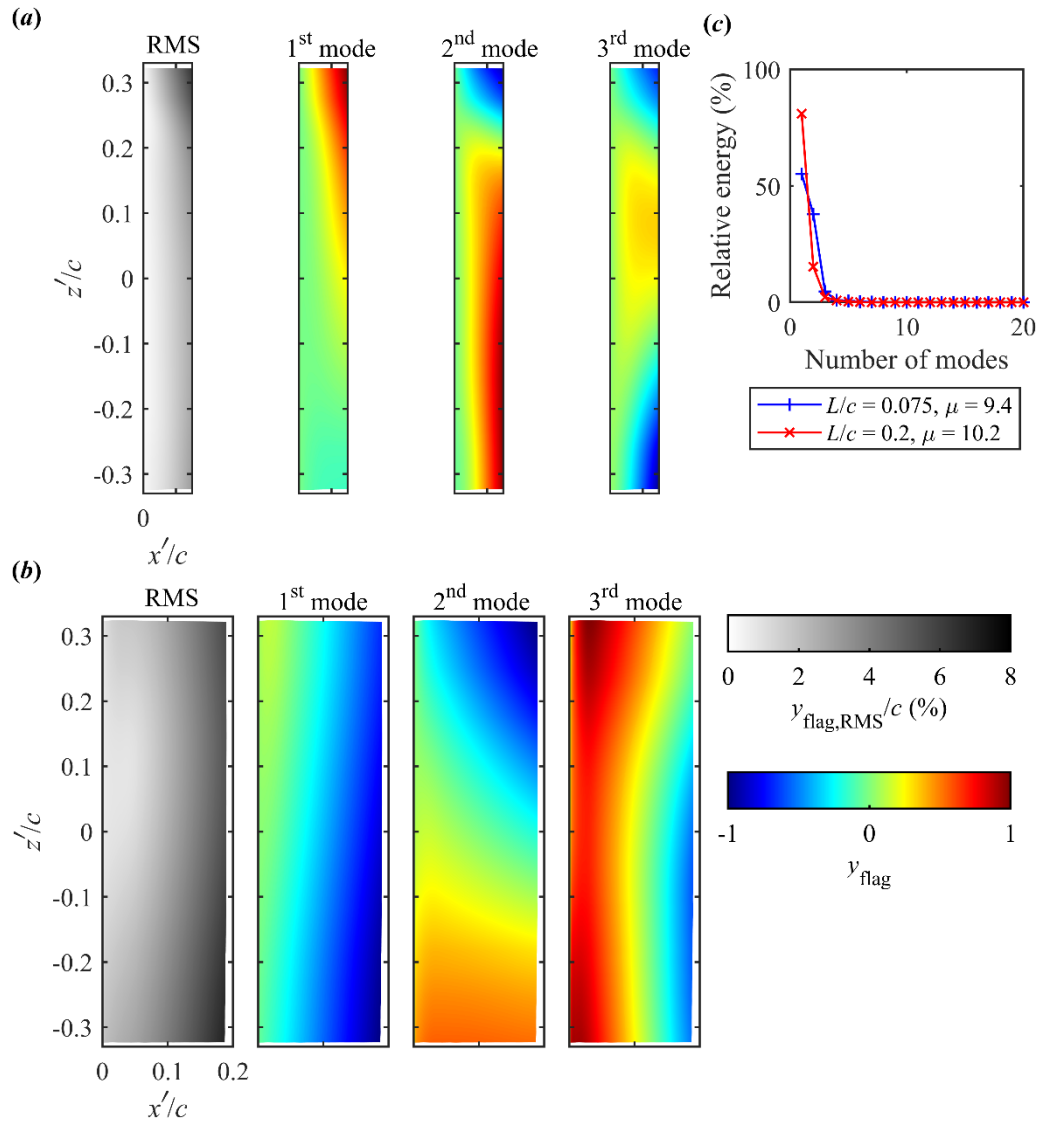

Figure 18: RMS and the first three POD modes of flag displacement fluctuations, (a) $L/c = 0.075$, (b) $L/c = 0.2$; and (c) relative energy as a function of mode number; $\alpha = 30°$, $\Lambda = 50°$.

In Figure 18, the RMS and the first three POD modes are compared for the $L/c = 0.075$ and $L/c = 0.2$ flags. The longer flag has much larger amplitude of oscillations. Clearly large amplitude oscillations of the flag do not necessarily produce high lift. The fraction of energy of the POD modes shown in part (c) reveals that the first mode has 81% of the total energy for the longer flag, in contrast to 55% of the first mode for the shorter flag. The two-point cross-correlation coefficient for the $L/c = 0.075$ and $L/c = 0.2$ flags for $\alpha = 30°$ is compared in Figure 19. The curves show similar trend that the cross-correlation coefficient decays continuously from the upstream edge to the downstream edge. However, the decay of the cross-correlation is much faster for the shorter flag. Despite the shorter flag having smaller amplitude and less coherent oscillations, it produces substantially larger lift enhancement.
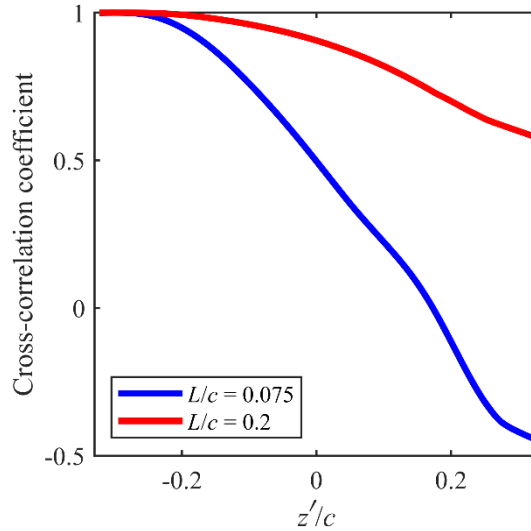

Figure 19: Two-point cross-correlation coefficient of the flag-tip displacement fluctuations as a function of flag spanwise distance for $L/c = 0.075$ and $L/c = 0.2$; $\alpha = 30°$, $\Lambda = 50°$.

Figure 20 presents a summary of the increase of the lift coefficient, flag dimensionless frequency, oscillation amplitude, and the Strouhal number based on the peak-to-peak amplitude as a function of the normalized length of the flags. The lift enhancement has a local maximum for $L/c = 0.1$, which has a dimensionless frequency of $fc/U_\infty \approx 0.8$. The flag vibration amplitude increases with increasing flag length. The longest flag with the largest amplitude of oscillations, but with a low dimensionless frequency, does not produce lift as high as the optimal flag length. The amplitude parameter fA/U_∞ is well correlated with the magnitude of the lift enhancement. Reviewing the effects of angle of attack,

mass ratio, and flag length (see Figures 11, 15, and 20), we conclude that the maximum lift enhancement is achieved when $fc/U_\infty \approx 0.8$ at a relatively large amplitude parameter fA/U_∞. Although the flag frequency, hence fc/U_∞ can be controlled by the appropriate choice of the flag properties, the amplitude parameter fA/U_∞ is not a control parameter as the peak-to-peak amplitude A is an outcome of the fluid-structure interaction.
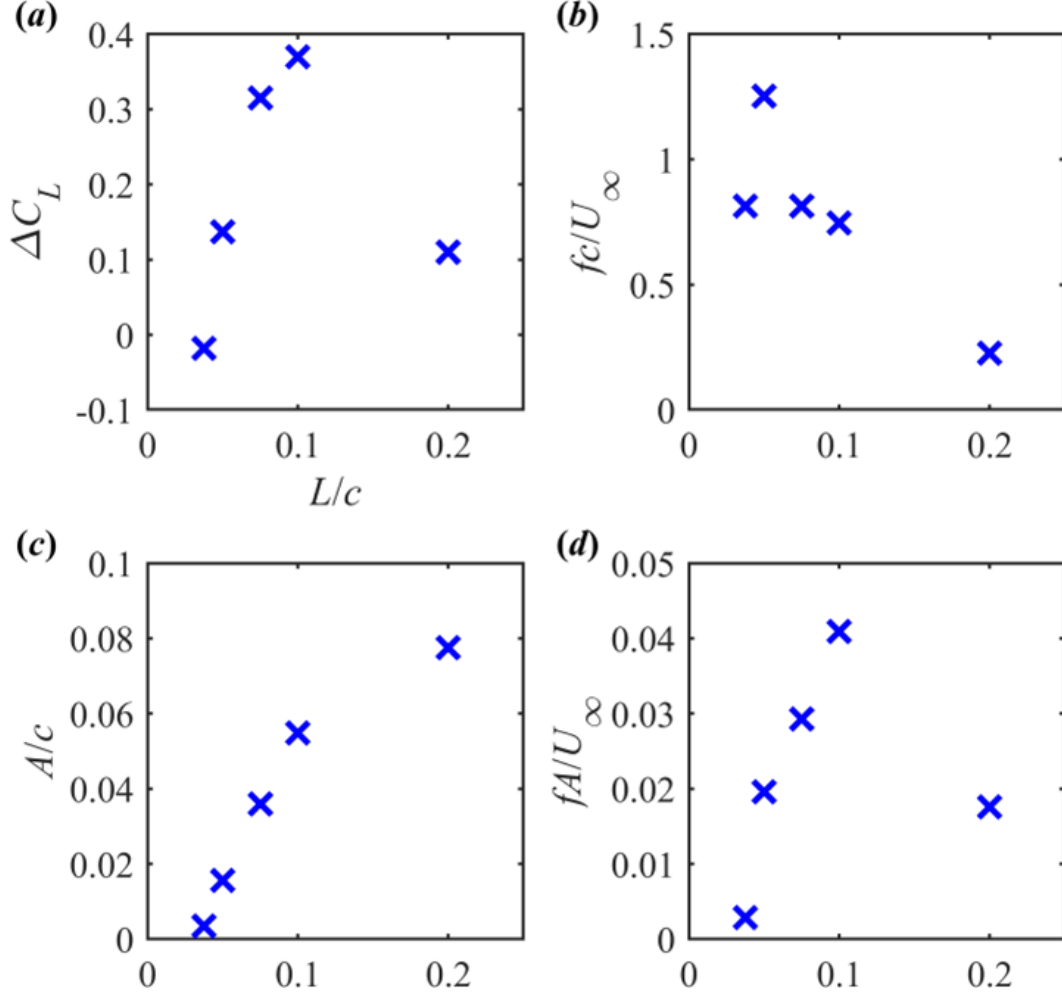

Figure 20: Variation of (a) change of lift coefficient, (b) dimensionless flag frequency, (c) normalized vibration amplitude, (d) Strouhal number based on the vibration amplitude as a function of normalized flag length L/c for $\alpha = 30°$, $\Lambda = 50°$.

As discussed above, the lift enhancement is maximized when fc/U_∞ is near unity for the flags tested for the $\Lambda = 50°$ delta wing. The previous studies with active flow control methods (such as unsteady blowing), small-amplitude wing motions and flexible wings identified a range of optimal dimensionless frequencies of 0.5 to 2.0 in the post-stall regime of nonslender delta wings as

summarized in the Introduction. To confirm that the optimal frequencies correspond to the natural shear layer instabilities for the clean wing in this investigation, the spectra of the hot-wire measurements are shown in Figure 21 at $\alpha = 30°$ for $\Lambda = 50°$. The spectra of velocity fluctuations
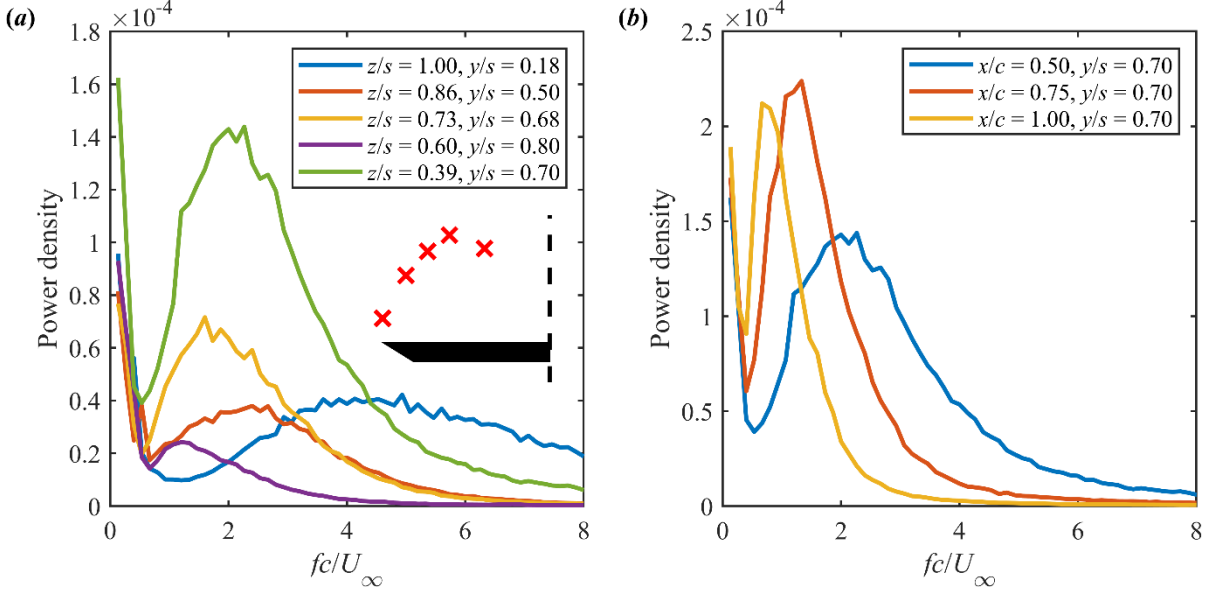

Figure 21: Spectra of velocity fluctuations measured on the clean wing at (a) $x/c = 0.5$ and (b) $z/s = 0.39$. The inset shows the measurement locations; $\alpha = 30°$, $\Lambda = 50°$.

along the shear layer at various locations for $x/c = 0.5$ are shown in Figure 21(a). Here, the distances are normalized by the local semi-span, s (see Figure 1 for the definition of the coordinate system). Dominant peaks are observed for all locations; however, they decrease as the measurement location moves inboard, due to the three-dimensional nature of the separated shear layer in a quasi-conical way. This is further supported in Figure 21(b), which shows the effect of streamwise distance on the spectra of the velocity fluctuations for the same y/s and z/s. As the streamwise distance is increased, the measured frequency decreases. These results are consistent with the previous experimental and computational studies for delta wings within a range of $\Lambda = 50°$ to $76°$ [5, 21, 22]. Gursul [21] reported that the dimensionless frequency fx/U_∞ is nearly constant for the delta wings in this range. (We note that the scaling changes for most slender wings with $\Lambda = 80°$ and $85°$ [23]). In our experiments, as the streamwise distance is increased to $x/c = 0.75$ to 1.00 (the range that the flag spans), the dominant

dimensionless frequencies approach unity, which agree with the observed optimal flag frequencies in the lift measurements.

F. Optimal flags

Even though the role of optimal frequency is clear, the results in Figures 11, 15, and 20 suggest that sufficiently large amplitude parameter fA/U_∞ is needed. To understand the effects of the parameters of fc/U_∞ and fA/U_∞ on the flow fields, we carried out PIV measurements for selected cases together with the clean wing (case 1). Table 1 shows the selected cases with the corresponding dimensionless frequency (fc/U_∞), excitation amplitude parameter (fA/U_∞), and lift coefficient enhancement (ΔC_L) at $\alpha = 30°$. These cases were selected based on the values of fc/U_∞ (in ascending order up to the optimal reduced frequency range) and fA/U_∞ (in increasing order until the maximum lift is observed in Table 1 for case 4, and then decreasing order). The variation of the parameter fA/U_∞ is similar to that of ΔC_L in Table 1.

<div align="center">Table 1: Summary of the PIV experiments.</div>

Case	fc/U_∞	fA/U_∞	ΔC_L	Note
1	–	–	–	Baseline case, clean wing
2	0.15	0.008	0.07	Nearly-rigid flag, $L/c = 0.1$, $\mu = 34.0$
3	0.44	0.029	0.25	Nearly-rigid flag, $L/c = 0.1$, $\mu = 16.4$
4	0.75	0.041	0.37	Nearly-rigid flag, $L/c = 0.1$, $\mu = 10.0$
5	0.81	0.029	0.32	Nearly-rigid flag, $L/c = 0.075$, $\mu = 9.4$
6	0.81	0.020	0.11	Compliant flag, $L/c = 0.05$, $\mu = 15.4$

The PIV measurements were performed in the x'-y' plane normal to the wing surface at the mid-span of the flags ($x/c = 0.75$). The time-averaged velocity magnitude contours superimposed with the time-averaged streamlines are shown in Figure 22. The phase-averaged flag shapes at the mid-span of the flags are also added. The red solid lines represent the flag when it is moving further away from the

wing surface whereas the black dashed-lines represent it when the flag is moving towards the wing surface. For the baseline case, the mean flow has a large recirculation region above the wing surface. With flags there are still recirculation regions in the measurement plane, even for case 4 with the largest lift increase. For case 4, we note that Figure 6 shows that there is a coherent streamwise vortex
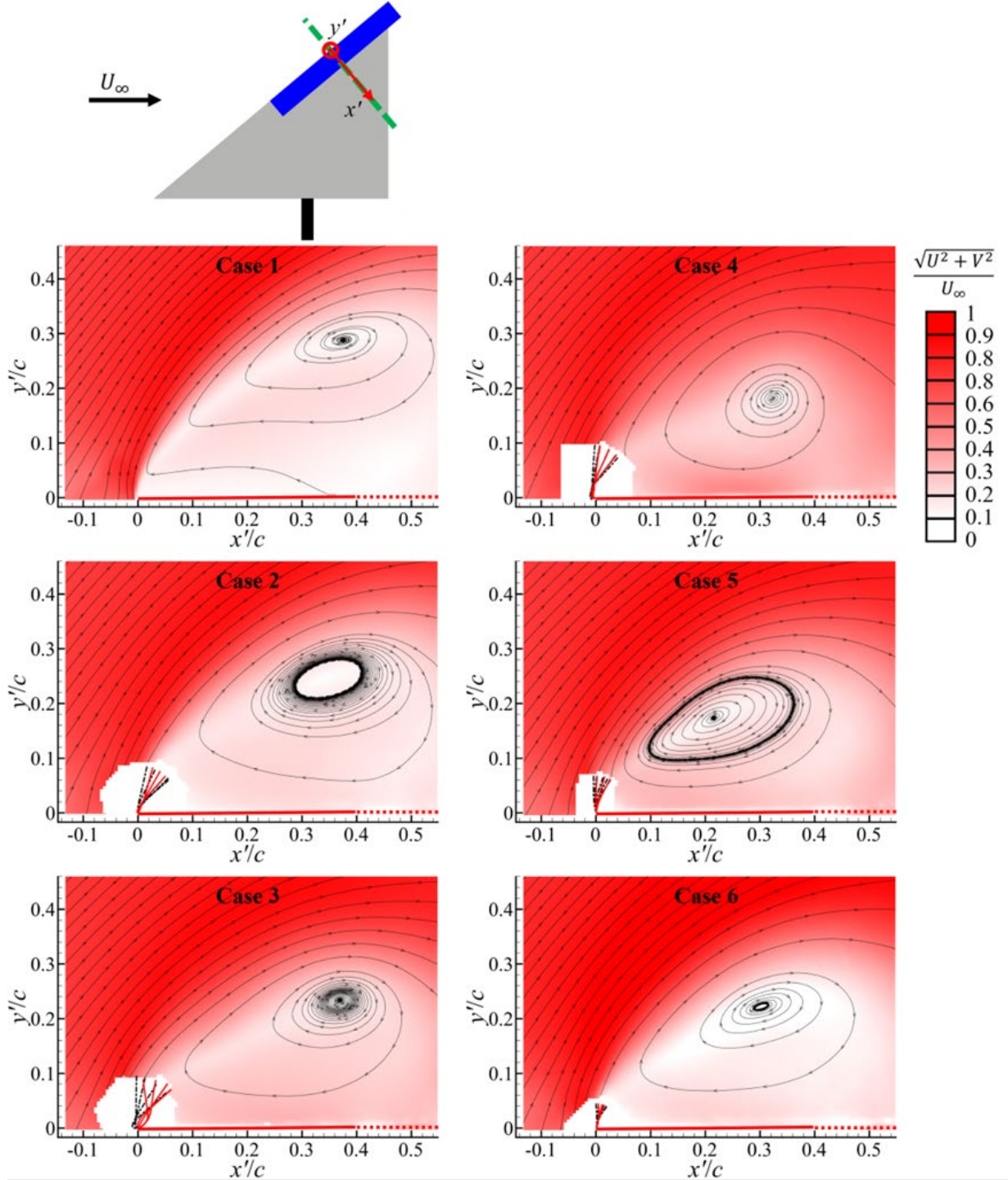

Figure 22: Time-averaged velocity magnitude contours superimposed with time-averaged streamlines and phase-averaged flag shapes in the x'-y' plane normal to the wing surface at the mid-span of the flags ($x/c = 0.75$), $\alpha = 30°$, $\Lambda = 50°$.
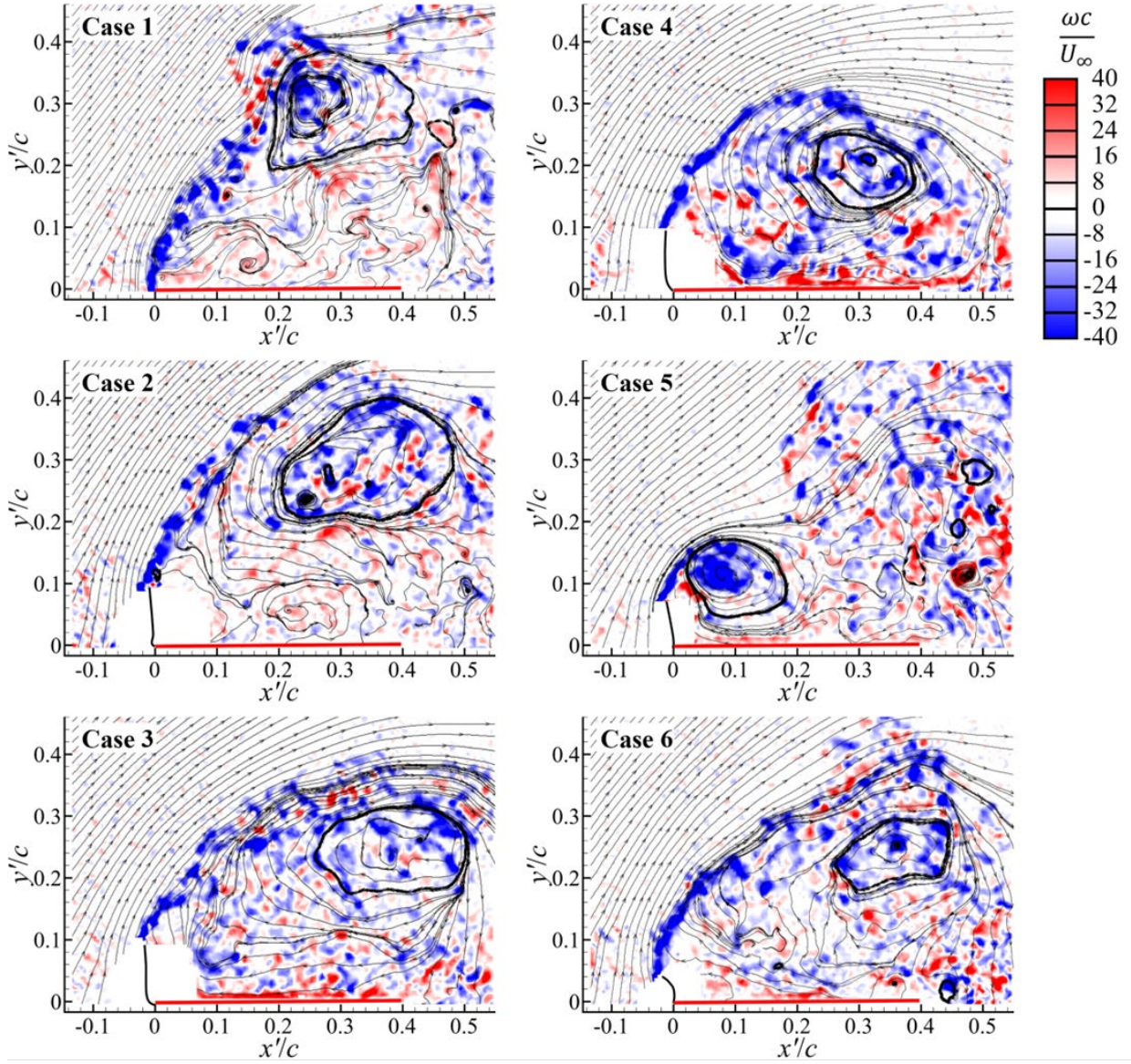
Figure 23: Instantaneous vorticity contours superimposed with instantaneous flag shapes when the flag tips are near maximum displacement in the x'-y' plane normal to the wing surface at the mid-span of the flags ($x/c = 0.75$), $\alpha = 30°$, $\Lambda = 50°$.

in upstream stations, but it undergoes vortex breakdown towards the trailing-edge. In Figure 22, the x'-y' plane normal to the wing surface at the mid-span of the flags ($x/c = 0.75$) cuts the trailing-edge ($x/c = 1$) near $x'/c \approx 0.4$. This is shown as the x'-axis changing from the solid line to the dotted line. Hence, the inboard sections closer to the symmetry plane are not visible. Nevertheless, the flow near the recirculation regions and the indications of the shear layer behavior inboard sections can be seen. For all cases with flags, the center of the recirculation regions moves closer to the leading-edge and

the wing surface than the baseline case. Case 4 has the largest magnitude of velocity in the recirculation region and close to the wing surface (this case has also the largest fA/U_∞ and the largest lift increase). The indication of the reattachment of the shear layer is in contrast to the no reattachment for the baseline case. Although the recirculation region for case 5 is even closer to the wing surface, it does not produce as large velocity magnitude inside the recirculation region and does not produce as high lift enhancement. This is due to the smaller value of the amplitude parameter fA/U_∞. For case 6, with the dimensionless frequency near the optimal range but with nearly half amplitude parameter as case 4, there is no reattachment to the wing surface.

Representative instantaneous vorticity contours superimposed with instantaneous flag shapes (extracted from the PIV images) in the x'-y' plane normal to the wing surface at the mid-span of the flags ($x/c = 0.75$) and $\alpha = 30°$ are shown in Figure 23 when the flag-tip is near maximum displacement. In contrast to the baseline case, the separated shear layer reattaches to the wing surface for case 4. For all other flags, there is no clear indication of reattachment at the corresponding instants. This is despite the fact that a small vortex is seen to develop near the flag-tip for case 5.

The first POD modes for each case are shown in Figure 24. For the baseline case, the first POD mode indicates natural vortex shedding. The wavelength of the vortical structures is estimated (assuming that the distance between two coherent vortices is roughly equal to the half of the wavelength) as $\lambda/c \approx 0.4$. For cases 2,3, and 4, the first mode looks like a "flapping mode" of the separated shear layer. All three cases have larger oscillations of the flag-tip compared to cases 5 and 6 (see the phase-averaged flag shapes in Figure 22). Only for case 4, the first POD mode gives an indication of the shear layer reattaching to the wing surface. For smaller-amplitude oscillations in case 5, which also has the highest dimensionless frequency, vortex roll-up and shedding are consistent with Figure 23. For the smallest amplitude of oscillation in case 6, periodic shedding is suggested by the first POD mode, but the discrete vortices in the instantaneous vorticity are not observed due to the very small

amplitude of the oscillations. The corresponding distributions of the relative energy of modes up to ten are shown in Figure 25. As expected, the baseline case has the least coherent flow and its first mode only accounts for 10% of the total energy. Case 4 is the most coherent flow, with the first mode having 32% of the total energy.
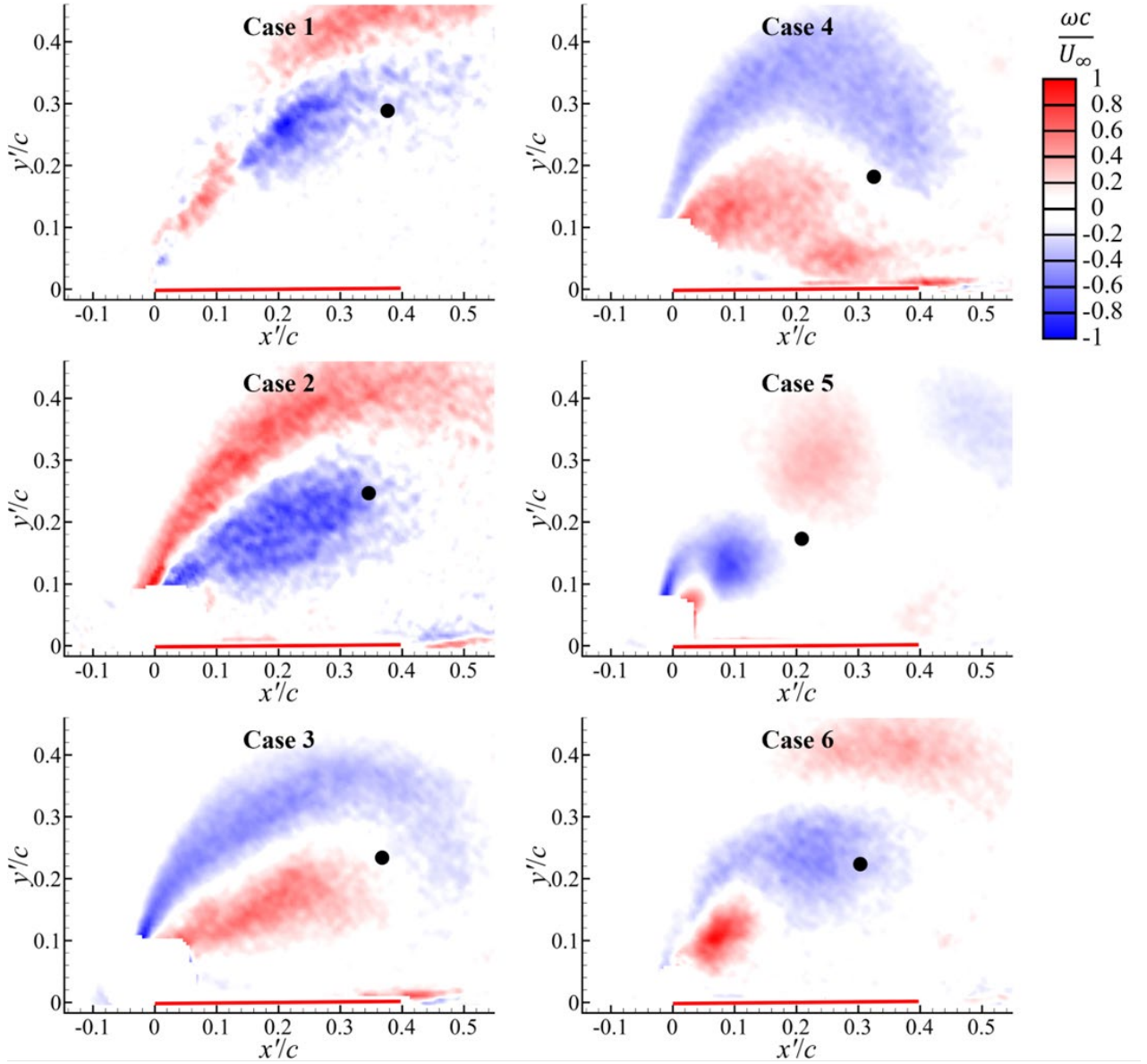

Figure 24: POD analysis of flow fields: contours of the first dominant vorticity modes in the *x'-y'* plane normal to the wing surface at the mid-span of the flags (*x/c* = 0.75), $\alpha = 30°$, $\Lambda = 50°$. The black dots indicate centers of the recirculation regions.
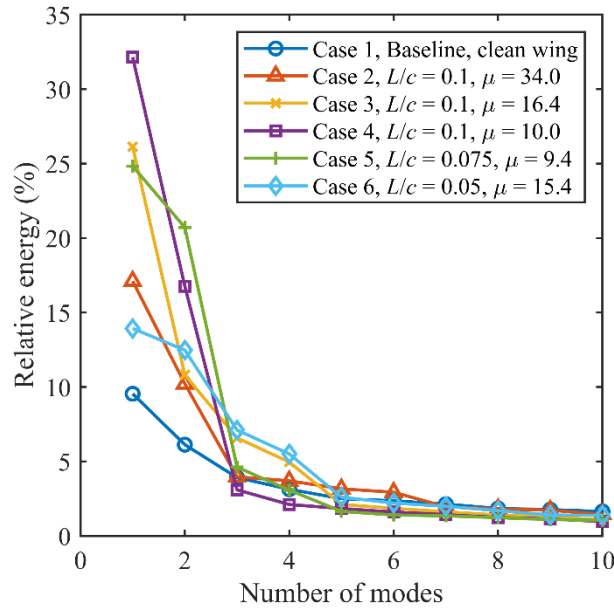
Figure 25: POD analysis of flow fields: fraction of energy as a function of mode number for the x'-y' plane normal to the wing surface at the mid-span of the flags ($x/c = 0.75$), $\alpha = 30°$, $\Lambda = 50°$.

G. Lower sweep angle of $\Lambda = 40°$

Similar force and flag deformation measurements were performed for the lower sweep angle of $\Lambda = 40°$. Figure 26 shows that, like the $\Lambda = 50°$ wing, increased lift and delayed stall are observed for flags with various mass ratio for a fixed value of $L/c = 0.1$. In this figure, the nearly-rigid flag with $\mu = 10.0$ and $L/c = 0.1$ has a maximum lift coefficient of $C_{L,max} = 1.10$ and a stall angle of $\alpha_s = 24°$ (versus $C_{L,max} = 1.07$ and $\alpha_s = 30°$ for the 50-deg sweep wing). Hence, the lift enhancement with attached flags seems equally effective for the lower sweep angle of $\Lambda = 40°$. The enhancements are significant: a 38% increase in the maximum lift coefficient and 4° delay of stall. There is a trend of slight decrease of the maximum lift coefficient with increasing mass ratio. Interestingly, even for the heaviest flag tested ($\mu = 34.0$, $L/c = 0.1$), a 17% enhancement in the maximum lift and a 4° stall delay are observed.

To compare the increase in the maximum lift coefficient with those for the $\Lambda = 50°$ wing as well as for the NACA0012 airfoil with attached flags, Figure 27 presents $\Delta C_{L,max}$ as a function of the dimensionless frequency. The comparisons between the three cases are made at the post-stall angles
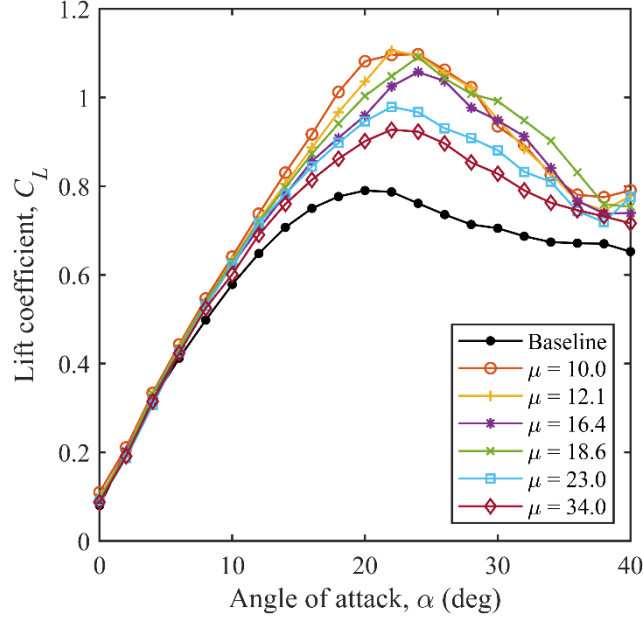
Figure 26: Time-averaged lift coefficient C_L as a function of angle of attack α for flags of length L/c = 0.1 with varying mass ratio; $\Lambda = 40°$.
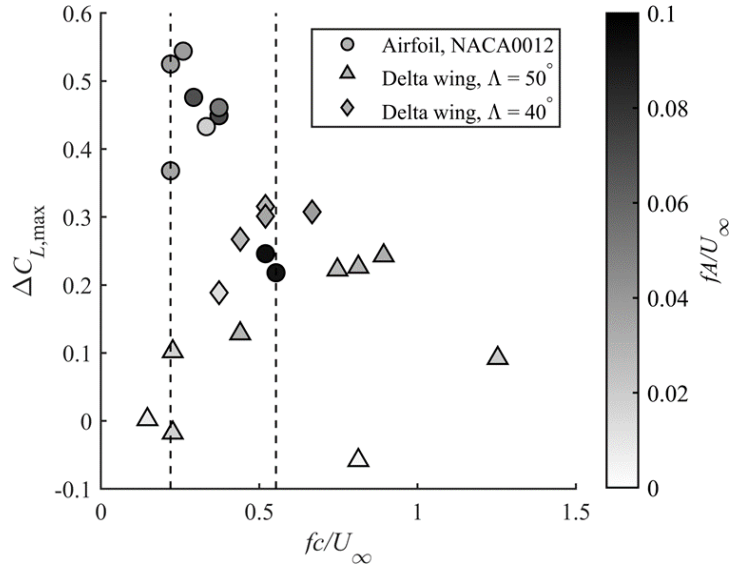

Figure 27: Change of maximum lift coefficient as a function of the dimensionless frequency. The data were colored according to the magnitude of the amplitude parameter fA/U_∞.

of attack at which the best improvements are attainable: $\alpha = 30°$ for the 50-deg sweep delta wing, $\alpha = 24°$ for the 40-deg sweep delta wing, and $\alpha = 20°$ for the NACA0012 airfoil [10]. The two vertical dashed lines indicate the range of the dimensionless frequency fc/U_∞ for the NACA0012 airfoil. This range is $fc/U_\infty = 0.22$ to 0.55, which corresponds to a modified Strouhal number of $fc\sin(\alpha)/U_\infty =$

0.075 to 0.19. As reported by Tan *et al*. [10], the upper and lower values correspond to the fundamental and the subharmonic of the wake instability. For the nominally two-dimensional case (zero sweep angle), the flags lock-in to the wake instability. The magnitude of the lift increase can be larger than those of nonslender delta wings when the flag frequency is near the subharmonic of the wake instability. The data in Figure 27 were colored according to the magnitude of the amplitude parameter fA/U_∞. Figure 27 reveals that the largest lift increases can be attained with relatively small values of the amplitude parameter fA/U_∞ in the lock-in range of the dimensionless frequency due to the absolute instability of the post-stall wakes.
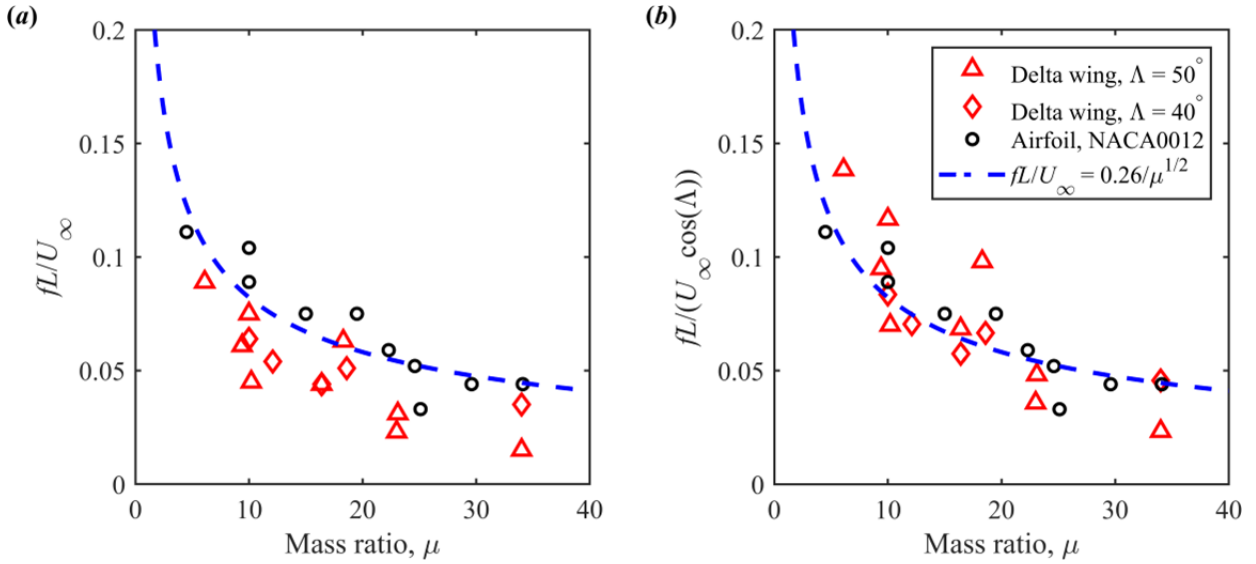

Figure 28: Dimensionless flag frequency as a function of flag mass ratio μ.

In contrast, for the nonslender delta wings, the data in Figure 27 reveal that the flag dimensionless frequencies vary in a wider range because there is no lock-in to the instabilities. It appears that there is an optimal range of $fc/U_\infty \approx 0.5$ to 0.8 for high lift. It is reported [24] that, even for a slender delta wing ($\Lambda = 75°$) at a very high angle of attack ($\alpha = 54°$), a highly coherent leading-edge vortex can be recovered with periodic excitation of the shear layer at an optimum dimensionless frequency around $fc/U_\infty \approx 1.0$. Also, levels of the amplitude parameter fA/U_∞ are moderate but sufficient to produce high lift. The existence of the optimal range of the dimensionless frequency for similar levels of the

amplitude parameter suggests a scenario of the excitation of the convective instability of the shear layers. Since there is lock-in phenomenon, the flag frequency, which is the natural frequency of the flag, can be controlled with the appropriate choice of the flag parameters.

In Figure 28(a) the flag dimensionless frequency fL/U_∞ is presented as a function of flag mass ratio μ for the airfoil and the two nonslender delta wings for the corresponding post-stall angles of attack. Also, a reduced order model [17] that predicts the natural frequency of two-dimensional flags in freestream is shown with a dashed line as:

$$fL/U_\infty = 0.26/\mu^{-1/2} \tag{4}$$

The dimensionless frequency fL/U_∞ for the nonslender delta wings is somewhat lower than that of the airfoil. This may be due to the effect of the leading-edge sweep on the flag frequencies. If the component of the freestream normal to the flag $U_\infty \cos(\Lambda)$ is used instead of U_∞ in the definition of the flag dimensionless frequency, i.e. $fL/U_\infty \cos(\Lambda)$, a better collapse for the airfoil and the two nonslender delta wings is seen in Figure 28(b).

IV. Conclusions

The aerodynamics of nonslender delta wings with flags attached to the leading-edge at post-stall angles of attack were investigated. Lift force, flag deformation fields, and flow fields were measured for two sweep angles, $\Lambda = 40°$ and $50°$. Significant increases in the maximum lift coefficient, the stall angle of attack and the increase of the lift coefficient at the stall angle with respect to the clean wing (exceeding 50%) were observed. The flow field measurements revealed that the flag oscillations caused the separated shear layer roll-up closer to the wing surface and the separated region became smaller compared to the clean wing case. For a flag that was placed between the mid-chord and trailing-edge, the separated flow reattached to the wing surface well upstream of the flag. A coherent vortex was observed over the upstream stations of the wing and subsequently underwent vortex-breakdown towards the trailing-edge. With regard to the possible applicability of this research, the

Flag oscillations were observed at pre-stall angles of attack of the clean wing as well but did not affect the time-averaged lift force regardless of the magnitude of the flag-tip velocity since the flow was already attached for the clean wing. In contrast, in the post-stall regime of the clean wing, despite the fact that the flag frequency remained unchanged, and the magnitude of the flag-tip velocity did not change much for a fixed flag length of $L/c = 0.1$, substantial lift increase reached a local maximum at $\alpha = 30°$ for $\Lambda = 50°$. The nearly constant frequency for the same flag across a wide range of angle of attack indicated that the flag oscillated at its natural frequency. Consequently, it was shown that the flag mass ratio was the main parameter that controlled the frequency of the flag oscillations. When the flag frequency approached the condition of fc/U_∞ near unity, the largest lift increase was achieved, while the amplitude parameter of the excitation, fA/U_∞, was also sufficiently large. Subsequently, by measuring the spectra of the velocity fluctuations, it was confirmed that the optimal frequencies corresponded to the natural shear layer instabilities of the clean wing. The flag frequency could also be changed by varying the flag length. Parametric investigation of various flags revealed that the optimal value was $L/c = 0.1$. Although longer flags have much larger amplitude of the oscillations, they have lower oscillation frequencies. The optimal lift enhancement for $L/c = 0.1$ also had the maximum dimensionless flag-tip velocity, fA/U_∞.

By varying the angle of attack, mass ratio, and flag length, we found that the maximum lift enhancement was achieved when $fc/U_\infty \approx 0.8$ at a relatively large amplitude parameter fA/U_∞. To understand the effects of these two parameters, selected cases with varying dimensionless frequency (fc/U_∞) and excitation amplitude parameter (fA/U_∞) were examined with PIV measurements. If the dimensionless frequency was within the optimal range and the excitation amplitude parameter was sufficiently large, it resulted in the reattachment of the shear layer, in contrast with the no reattachment

for the baseline case at $\alpha = 30°$. The POD analysis also confirmed that the optimal excitation substantially improved the coherency of the separated flow.

The lift enhancement was equally effective for the lower sweep angle of $\Lambda = 40°$. The effects of dimensionless frequency (fc/U_∞) and excitation amplitude parameter (fA/U_∞) on the maximum lift coefficient were compared for the NACA0012 airfoil and the nonslender delta wings with $\Lambda = 40°$ and $50°$. For the airfoil case, the flag oscillation frequency was locked to the wake instability and the maximum lift increase attainable was larger than those of the delta wings. This was due to the lock-in with the absolute instability of the post-stall wakes. In contrast, for the nonslender delta wings, there is an optimal range of the dimensionless frequency for high lift. In this case, the flags' natural frequency could be controlled with the appropriate choice of the flag properties. The main mechanism for lift increase is through the shear layer excitation (convective instability), which is different from the wake resonance for airfoils and high-aspect-ratio wings at the post-stall angles of attack.

Acknowledgement

References

[1] Gursul, I., Wang, Z., Vardaki, E., "Review of flow control mechanism of leading-edge vortices". *Progress in Aerospace Sciences,* Vol. 43, No. 7-8, 2007, pp. 246-270.
DOI: https://doi.org/10.1016/j.paerosci.2007.08.001

[2] Margalit, S., Greenblatt, D., Seifert, A., and Wygnanski, I., "Delta Wing Stall and Roll Control Using Segmented Piezoelectric Fluidic Actuators," *Journal of Aircraft*, Vol. 42, No. 3, 2005, pp. 698–709.
DOI: https://doi.org/10.2514/1.6904

[3] Williams, N.M., Wang, Z., Gursul, I., "Active Flow Control on a Nonslender Delta Wing". *Journal of Aircraft,* Vol. 45, No. 6, 2008, pp. 2100-2110.

DOI: https://doi.org/10.2514/1.37486

[4] Gad-el-Hak, M., Blackwelder, R.F., "Control of the Discrete Vortices from a Delta Wing". *AIAA Journal,* Vol. 25, No. 8, 1987, pp. 1042-1049.

DOI: https://doi.org/10.2514/3.9740

[5] Taylor, G., Wang, Z., Vardaki, E., Gursul, I., "Lift Enhancement over Flexible Nonslender Delta Wings", *AIAA Journal*, Vol. 45, No. 12, 2007, pp. 2979-2993.

DOI: https://doi.org/10.2514/1.31308

[6] Cipolla, K.M., Rockwell, D., "Flow Structure on Stalled Delta Wing Subjected to Small Amplitude Pitching Oscillations", *AIAA Journal,* Vol. 33, No. 7, 1995, pp.1256-1262.

DOI: https://doi.org/10.2514/3.12548

[7] Yaniktepe, B., Rockwell, D., "Flow Structure on a Delta Wing of Low Sweep Angle", *AIAA Journal*, Vol. 42, No. 3, 2004, pp. 513–523.

DOI: https://doi.org/10.2514/1.1207

[8] Vardaki, E., Wang, Z., Gursul, I., "Flow Reattachment and Vortex Re-formation on Oscillating Low-Aspect-Ratio Wings", *AIAA Journal,* Vol. 46, No. 6, 2008, pp. 1453-1462.

DOI: https://doi.org/10.2514/1.32233

[9] Tan, J., Wang, Z., Gursul, I., "Self-excited flag vibrations produce post-stall flow control", *Physical Review Fluids,* Vol. 6, No. 10, 2021, L102701.

DOI: https://doi.org/10.1103/PhysRevFluids.6.L102701

[10] Tan, J., Wang, Z., Gursul, I., "Post-stall flow control on aerofoils by leading-edge flags", 2023, *Journal of Fluid Mechanics*, vol. 972, A4.

DOI: https://doi.org/10.1017/jfm.2023.678

[11] Tan, J., Wang, Z., Gursul, I., "Aerodynamics of finite wings with leading-edge flags", 2023, *under review*.

[12] Huerre, P. & Monkewitz, P.A., "Local and Global Instabilities in Spatially Developing Flows", *Annual Review of Fluid Mechanics*, Vol. 22, 1990, pp. 473-537.

DOI: https://doi.org/10.1146/annurev.fl.22.010190.002353

[13] Moffat, R.J., "Using Uncertainty Analysis in the Planning of an Experiment", *Journal of Fluids Engineering,* Vol. 107, No. 2, 1985, pp. 173-178.

DOI: https://doi.org/10.1115/1.3242452

[14] Peters, W.H., Ranson, W.F., "Digital imaging techniques in experimental stress analysis", *Optical Engineering,* Vol. 21, No. 3, 1982, 213427.

DOI: https://doi.org/10.1117/12.7972925

[15] Chu, T.C., Ranson, W.F., Sutton, M.A., "Applications of Digital-Image-Correlation Techniques to Experimental Mechanics", *Experimental Mechanics,* Vol. **25,** 1985, pp. 232-244.

DOI: https://doi.org/10.1007/BF02325092

[16] Rojratsirikul, P., Genc, M.S., Wang, Z., Gursul, I., "Flow-induced vibrations of low aspect ratio rectangular membrane wings", *Journal of Fluids and Structures,* Vol. 27, No. 8, 2011, pp. 1296-1309.

DOI: https://doi.org/10.1016/j.jfluidstructs.2011.06.007

[17] Zhang, Z., Wang, Z., Gursul, I., "Post-stall flow control with upstream flags", *Experiments in Fluids*, Vol. 63, 2022, Article number: 179.

DOI: https://doi.org/10.1007/s00348-022-03528-0

[18] Gurka, R., Liberzon, A., Hetsroni, G., "POD of vorticity fields: A method for spatial characterization of coherent structures", *International Journal of Heat and Fluid Flow,* Vol. 27, No. 3, 2006, pp. 416-423.

DOI: https://doi.org/10.1016/j.ijheatfluidflow.2006.01.001

[19] Wang, J.J., Lu, S.F., "Effects of leading-edge bevel angle on the aerodynamic forces of a nonslender 50° delta wing", *The Aeronautical Journal,* Vol. 109, No. 1098, 2005, pp. 403-407.

DOI: https://doi.org/10.1017/S0001924000000828

[20] Bendat, J.S., Piersol, A.G., *Random Data: Analysis and Measurement Procedures*. 4th ed. Hoboken, New Jersey: Wiley, 2010.

DOI: https://doi.org/10.1002/9781118032428

[21] Gursul, I. "Unsteady flow phenomena over delta wings at high angle of attack", *AIAA Journal*, Vol. 32, No. 2, 1994, pp. 225–231.

DOI: https://doi.org/10.2514/3.11976

[22] Gordnier, R.E. & Visbal, M. R. "Unsteady vortex structure over a delta wing", *Journal of Aircraft*, Vol. 31, No. 1, 1994, pp. 243–248.

DOI: https://doi.org/10.2514/3.46480

[23] Ma, B.F. Wang, Z. and Gursul, I. "Symmetry breaking and instabilities of conical vortex pairs over slender delta wings", *Journal of Fluid Mechanics*, Vol. 832, 2017, pp. 41-72.

DOI: https://doi.org/10.1017/jfm.2017.648

[24] Gu, W., Robinson, O. and Rockwell, D. "Control of Vortices on a Delta Wing by Leading-Edge Injection", *AIAA Journal,* Vol. 31, No. 7, July 1993, pp.1177-1186.

DOI: https://doi.org/10.2514/3.11749